FERMILAB-PUB-09-865-A

Accepted for publication in *The Astrophysical Journal*
Preprint typeset using LaTeX style emulateapj v. 03/07/07

arXiv:0907.4524v1 [astro-ph.CO] 26 Jul 2009

# THE CARNEGIE SUPERNOVA PROJECT: FIRST NEAR-INFRARED HUBBLE DIAGRAM TO Z∼0.7*

Wendy L. Freedman[1], Christopher R. Burns[1], M. M. Phillips[2], Pamela Wyatt[1], S. E. Persson[1], Barry F. Madore[1], Carlos Contreras[2], Gaston Folatelli[2,3],E Sergio Gonzalez[2], Mario Hamuy[3], Eric Hsiao[4], Daniel D. Kelson[1], Nidia Morrell[2], D. C. Murphy[1], Miguel Roth[2], Maximilian Stritzinger[2], Laura Sturch[1], Nick B. Suntzeff[21] P. Astier[6], C. Balland[6,7], Bruce Bassett[8], Luis Boldt[2], R. G. Carlberg[9], Alexander J. Conley[9], Joshua A. Frieman[10,11,12], Peter M. Garnavich[13], J. Guy[6], D. Hardin[6], D. Andrew Howell[14,15], Richard Kessler[16,11], Hubert Lampeitl[5], John Marriner[10], R. Pain[6], Kathy Perrett[9], N. Regnault[6], Adam G. Riess[17], Masao Sako[16,18], Donald P. Schneider[19], Mark Sullivan[20], and Michael Wood-Vasey[22]

*Accepted for publication in The Astrophysical Journal*

## ABSTRACT

The Carnegie Supernova Project (CSP) is designed to measure the luminosity distance for Type Ia supernovae (SNe Ia) as a function of redshift, and to set observational constraints on the dark energy contribution to the total energy content of the Universe. The CSP differs from other projects to date in its goal of providing an $I$-band *rest-frame* Hubble diagram. Here we present the first results from near-infrared (NIR) observations obtained using the Magellan Baade telescope for SNe Ia with $0.1 < z < 0.7$. We combine these results with those from the low-redshift CSP at $z < 0.1$ (Folatelli et al. 2009). In this paper, we describe the overall goals of this long-term program, the observing strategy, data reduction procedures, and treatment of systematic uncertainties. We present light curves and an $I$-band Hubble diagram for this first sample of 35 SNe Ia and we compare these data to 21 new SNe Ia at low redshift. These data support the conclusion that the expansion of the Universe is accelerating. When combined with independent results from baryon acoustic oscillations (Eisenstein et al. 2005), these data yield $\Omega_m = 0.27 \pm 0.02$ (statistical), and $\Omega_{DE} = 0.76 \pm 0.13$ (statistical) $\pm 0.09$ (systematic), for the matter and dark energy densities, respectively. If we parameterize the data in terms of an equation of state, $w$ (with no time dependence), assume a flat geometry, and combine with baryon acoustic oscillations, we find that $w = -1.05 \pm 0.13$ (statistical) $\pm$ 0.09 (systematic). The largest source of systematic uncertainty on $w$ arises from uncertainties in the photometric calibration, signaling the importance of securing more accurate photometric calibrations for future supernova cosmology programs. Finally, we conclude that either the dust affecting the luminosities of SNe Ia has a different extinction law ($R_V = 1.8$) than that in the Milky Way (where $R_V = 3.1$), or that there is an additional intrinsic color term with luminosity for SNe Ia, independent of the decline rate. Understanding and disentangling these effects is critical for minimizing the systematic uncertainties in future SN Ia cosmology studies.

*Subject headings:* cosmology: observations – cosmology: distance scale – supernovae: general

## 1. INTRODUCTION

Observations of high-redshift Type Ia supernovae (SNe Ia) currently provide the best evidence for an accelerating universe (Riess et al. 1998;

*THIS PAPER INCLUDES DATA GATHERED WITH THE 6.5 METER MAGELLAN TELESCOPES LOCATED AT LAS CAMPANAS OBSERVATORY, CHILE.

[1] Carnegie Observatories, 813 Santa Barbara St, Pasadena, CA, 91101, USA
[2] Carnegie Institution of Washington, Las Campanas Observatory, Colina El Pino, Casilla 601, Chile
[3] Universidad de Chile, Departmento de Astronomia, Casilla 36-D, Santiago, Chile
[4] Department of Physics and Astronomy, University of Victoria, PO Box 3055, Stn CSC, Victoria, BC V8W 3P6, Canada
[5] Institute of Cosmology and Gravitation, University of Portsmouth, Portsmouth, P01 3FX, UK
[6] LPNHE, CNRS-IN2P3 and Universités Paris VI & VII,4 place Jussieu, 75252 Paris Cedex 05, France
[7] APC, Collège de France, 11 place Marcellin Berthelot, 75005 Paris, France
[8] Department of Mathematics and Applied Mathematics, University of Cape Town, Rondebosch 7701, South Africa and South African Astronomical Observatory, P.O. Box 9, Observatory 7935, South Africa
[9] Department of Astronomy, University of Toronto, 60 St. George St., Toronto, M5S 3H8, ON, Canada
[10] Center for Particle Astrophysics, Fermi National Accelerator Laboratory, P.O. Box 500, Batavia, IL 60510, USA
[11] Enrico Fermi Institute, University of Chicago, 5640 South Ellis Avenue, Chicago, IL 60637, USA
[12] Department of Astronomy and Astrophysics, The University of Chicago, 5640 South Ellis Avenue, Chicago, IL 60637, USA
[13] University of Notre Dame, 225 Nieuwland Science, Notre Dame, IN46556-5670, USA
[14] Las Cumbres Observatory Global Telescope Network, 6740 Cortona Dr., Suite 102, Goleta, CA 93117, USA
[15] Department of Physics, University of California, Santa Barbara, Broida Hall, Mail Code 9530, Santa Barbara, CA 93106-9530, USA
[16] Kavli Institute for Cosmological Physics, The University of Chicago, 5640 South Ellis Avenue Chicago, IL 60637, USA
[17] Department of Physics and Astronomy, Johns Hopkins University, Baltimore, MD and Space Telescope Science Institute, Baltimore, MD, USA
[18] Department of Physics and Astronomy, University of Pennsylvania, 209 South 33rd Street, Philadelphia, PA 19104, USA
[19] Department of Astronomy and Astrophysics, Pennsylvania State University, 525 Davey Laboratory, University Park, PA 16802, USA
[20] Department of Astrophysics, University of Oxford, Keble Road, Oxford OX1 3RH, UK
[21] Physics Department, Texas A&M University, College Station, TX, 77843, USA
[22] Department of Physics and Astronomy, 3941 O'Hara St, University of Pittsburgh, Pittsburgh, PA 15260, USA

Perlmutter et al. 1999; Knop et al. 2003; Astier et al. 2006; Wood-Vasey et al. 2007). Independently, the Wilkinson Microwave Anisotropy Probe (WMAP) measurements of fluctuations in the cosmic microwave background (CMB) (Spergel et al. 2003, 2007); detections of acoustic oscillations in the matter density spectrum (Eisenstein et al. 2005); as well as the comparison of Hubble expansion ages from the Hubble Key Project (Freedman et al. 2001) with the ages of Milky Way globular clusters (Krauss & Chaboyer 2003), have all led to the growing body of evidence for a dark-energy component to the overall mass-energy density of the Universe (see also Frieman et al. (2008) for a recent review). The above studies yield results consistent with a flat universe where the sum of the dark energy and matter densities $\Omega_{DE} + \Omega_m = 1$, and where $\Omega_{DE} \sim 0.7$, with a matter density $\Omega_m \sim 0.3$.

At present, a physical understanding of this dark energy component remains elusive, and there is a wide variety of possible alternatives ranging from the cosmological constant, as originally proposed by Einstein in 1917; a decaying scalar field; or perhaps even a modification of general relativity. A convenient measure is $w$, the ratio of pressure $P$ to energy density $\rho$, where $w = P/\rho$. In the case of a cosmological constant, $w = -1$. The time evolution of $w$ is not known at present. Given our currently limited understanding of this critical component of the Universe, it is clear that further observational and experimental data are needed to constrain and characterize the properties of dark energy.

SNe Ia show a relation between peak brightness and rate of decline, in addition to color (or reddening). Accounting for these correlations yields a dispersion in the Hubble diagram of about 7% in distance (Phillips 1993; Hamuy et al. 1995; Riess et al. 1996; Hamuy et al. 1996a; Astier et al. 2006). As more and more SNe Ia are discovered and the statistical uncertainties in this method are decreased, the challenge becomes understanding and controlling the remaining systematic uncertainties, as well as testing for currently unknown systematic effects. A well-known systematic is reddening and extinction due to dust, and there may potentially be differences due to chemical composition and age of the progenitors or their environment. The requirement for increasing measurement accuracy, the lack of a detailed theoretical understanding of SN Ia, the fact that most observations have been made at rest-frame optical and ultraviolet colors (where reddening uncertainties are large), the difficulty of obtaining accurate K- and spectral-corrections, all point to the need to characterize and decrease these systematic errors and uncertainties. As other errors have been reduced over time, what were relatively small effects previously have now become increasingly important as the required precision in cosmology has risen.

Observations of SNe Ia at near-infrared (NIR) wavelengths offer several advantages in minimizing a number of systematic effects (most notably reddening), as well as providing an additional, independent probe of the expansion history. We make use of the $Y$ band, centered near 1.035 $\mu$m (Hillenbrand et al. 2002), which falls in between the traditionally classified optical and infrared spectral regimes. The $Y$ and $J$ (1.25 $\mu$m) bands provide a means of obtaining *rest-frame* $I$-band magnitudes for SNe Ia in the redshift range 0.1 to 0.7, an interval covering the time at which the influence of dark energy begins to dominate the expansion. Hence, NIR observations offer an important opportunity both to minimize systematic uncertainties and yield an independent Hubble diagram.

Aside from a few observations published by Riess et al. (2000) and Nobili et al. (2005), rest-frame $I$-band measurements have not yet been routinely undertaken at higher redshifts because at z$\sim$0.25 the $I$-band is redshifted beyond the CCD sensitivity limit at red wavelengths. A further challenge to NIR photometry obtained from the ground is that the sky background is much greater than at optical wavelengths. As a consequence, observing distant SNe Ia in the NIR is expensive in telescope time. However, since current searches to find SNe Ia now yield extensive optical coverage of the light curves, the decline rates and time of maximum light are already well defined, so that fewer observations are required to derive NIR light curve parameters accurately. With the availability of 6.5-meter class telescopes and NIR arrays, a NIR study of SNe Ia at z $>$ 0.1 has now become feasible.

Ongoing optical surveys aimed at discovering large samples of SNe Ia are signficantly decreasing the statistical uncertainties in SN Ia cosmology measurements, while simultaneously aiming to reduce the systematic errors. The CSP is complementary to these studies; that is, it is not designed to rival optical surveys on numbers of objects and statistical errors, but rather it is more focused on follow-up observations critical to testing for and minimizing systematic uncertainties. These follow-up observations (multiple wavelengths at low redshift, and NIR observations at higher redshifts) require more observing time per individual SN Ia. An understanding of the systematic errors is a critical goal for all SN Ia programs.

To date, as part of the high-redshift CSP, we have obtained NIR observations of 80 SNe Ia. Subsequent host-galaxy observations have been obtained for 71 objects and we have fully analyzed 35 objects, the sample for which photometry, light curves and a preliminary Hubble diagram are presented in this paper.

## 2. THE CARNEGIE SUPERNOVA PROJECT

The CSP is an umbrella name for our two coordinated SN programs: one being carried out at the Las Campanas 1 m Swope and 2.5 m Dupont telescopes for low (0<z<0.1) redshift objects, and the other using the Magellan Baade 6.5 m telescope at higher (0.1<z<0.7) redshifts. Preliminary results from the low-redshift part of this project have been reported in Hamuy et al. (2006), Folatelli et al. (2006) and Phillips et al. (2007); the most recent results are presented in two companion papers (Contreras et al. 2009; Folatelli et al. 2009). The CSP is not a SN *search* program; rather as described below, as well as in Hamuy et al. (2006), we are using the facilities of the Las Campanas Observatory, in coordination with several on-going search programs elsewhere, to provide detailed and immediate *follow-up* observations of newly-discovered SNe.

### 2.1. *Goals*

Overall, the CSP is focused on obtaining observations of SNe Ia falling in the redshift range 0<z<0.7. As described in Hamuy et al. (2006), at low redshifts we are currently obtaining 10-filter ($uBVgriYJHK_s$) photometry with excellent time sampling and optical spectroscopy to provide a database for the determination of the Hubble constant, accurate K-corrections, comparison with theoretical models of SNe Ia, and a fundamental dataset for comparison with high redshift. At high redshifts, as described in this current paper, we are obtaining $YJ$ data near maximum light. The NIR data, in conjunction with optical photometry (being obtained as part of the search programs), allow the determination of reddening corrections and a rest-frame $I$-band Hubble diagram. One of the key goals of the CSP is to minimize the effects of reddening in the Hubble diagram, and ensure that the *rest-frame* ($BVi$) bandpasses, being observed at low redshift, match those for a sample at higher redshift, so that reddening corrections can be applied in a uniform way. Ultimately the goal is to measure accurate luminosity distances to better constrain cosmological models. Assuming a model including dark energy, the goal is to characterize the acceleration of the Universe and constrain the equation of state, $w$, to a precision *and accuracy* of $\pm 10\%$.

### 2.2. *"I-band" filter nomenclature*

There are many "I-band" filters in current use. We distinguish here between the Kron-Cousins $I$-band, the SNLS MegaCam $i_M$-band (based on Landolt standards calibrated to Vega), and the SDSS-II $i_S$-band (based on a calibration tied to four subdwarfs, Smith et al. (2002)). Our Las Campanas natural $i$-band calibration is also tied to Smith et al. The central wavelengths of these (and other) passbands are defined in Table 1. In this paper, we also refer to a generic 'I-band' when speaking collectively about observations in the NIR wavelength range $\sim 8000\AA$.

### 2.3. *I-band Light Curves SNe Ia*

The form of NIR light curves for SNe Ia differs from those at optical wavelengths. At $IYJH$ and $K$, the light curves show a minimum following maximum light, followed by an additional secondary maximum, less luminous than the primary peak (e.g., Elias et al. 1985; Hamuy et al. 1996b; Meikle 2000; Krisciunas et al. 2001; Nobili et al. 2005). This secondary maximum is thought to be the result of a sudden drop in the mean opacity in the SN ejecta (Pinto & Eastman 2000; Kasen 2006). In Figure 1, we show some examples of $i$-band light curves for four well-observed, nearby SNe Ia from the low-z CSP sample. Our strategy for the high-redshift CSP is to obtain $i$ photometry covering the first peak only, and to avoid the (fainter) secondary maximum. The optical surveys already provide measurements of the decline rate in the $B$ band, so duplication of these data is not required. The median start and end times of our observations are 0 and +12 days with respect to observed $i$-band maximum, respectively. In this paper, unless otherwise noted, we refer to the observed (not rest) frame time.

### 2.4. *Targets*

There have been four on-going SN search programs with which the CSP has been actively collaborating. At low redshifts (z < 0.1), we are collaborating with the Lick Observatory Supernova Search (LOSS), as described in Hamuy et al. (2006). For intermediate redshifts (0.1 < z < 0.4), we have been collaborating with the Sloan Digital Sky Survey II (SDSSII), while the CFHT Legacy Survey (SNLS) and ESSENCE found SNe Ia out to higher redshifts (0.1 < z < 0.7). The three surveys relevant to this higher-redshift study are described briefly below.

#### 2.4.1. *Sloan Digital Sky Survey (SDSS) II*

An extension to the Sloan Digital Sky Survey (York et al. 2000), the SDSS-II,[23] (Sako et al. 2008; Frieman et al. 2008) has completed a three-year rolling search program using the 2.5 m SDSS telescope to discover intermediate redshift (0.05 < z < 0.35) SNe Ia in a 300 square degree southern equatorial field, obtaining multicolor ($ugriz$) photometry with a cadence of ∼2-5 days. The data were obtained during the months of September through November 2005-2007. Spectra to determine redshifts and types for the SDSSII candidates were obtained with several telescopes with a range of apertures. Photometry for the 130 spectroscopically confirmed SNe Ia from the 2005 season have been presented in Holtzman et al. (2008).

#### 2.4.2. *CFHT Legacy Survey (SNLS)*

The Supernova Legacy Survey[24], a Canadian/French collaboration, used the CFHT and the 1 square-degree camera (MegaCam) to obtain deep optical ($u'g'r'i'z'$) images for four fields, each of approximately one square degree around the equator (Astier et al. 2006), beginning in February, 2003. The SNLS was also a rolling search program in which each field was revisited every second night during a 5-month campaign each semester for a total of five years. Spectroscopic follow-up for the SNLS candidates was obtained at the 10 m Keck telescope, the 8 m Very Large Telescope (VLT), the 8 m Gemini North and South telescopes, as well as the Magellan telescopes. In their first year of operation, they discovered 91 SNe Ia, and published data for a sample of 71 SNe Ia with redshifts 0.1 < z < 1.1. In total, about 450 SNe Ia have been discovered.

#### 2.4.3. *ESSENCE*

ESSENCE[25] completed its survey using the 4 m CTIO Blanco telescope and MOSAIC II wide-field camera covering equatorial fields at $VRI$ wavelengths over the redshift range between 0.15 < z < 0.75 (Matheson et al. 2005; Miknaitis et al. 2007). The goal was to provide optical light curves for about 200 Type Ia SNe Ia over 5 years (2002-2007). ESSENCE was scheduled for 30 half nights during a 3-month (October - December) campaign each year. The observing was centered on new moon, and was scheduled every other night, for a span of 20 days, with a gap of 10 bright nights per month. Spectroscopic follow-up for the ESSENCE candidates was obtained at Gemini North and South, Keck, the VLT, MMT, and Magellan telescopes. At the time of writing, ESSENCE has published observations for 102 SNe Ia (Wood-Vasey et al. 2007).

[23] http://www.sdss.org
[24] http://www.cfht.hawaii.edu/Science/CFHLS
[25] http://www.ctio.noao.edu/essence

### 2.5. *CSP Magellan Follow-up Observations*

Our follow-up Magellan observations consist of $Y$- and/or $J$-band images. We chose not to observe at $H$-band because of the increased sky background produced by atmospheric OH airglow emission. Optical photometry for this sample of SNe Ia was obtained during the course of the original surveys (SDSS-II, ESSENCE, SNLS), and was not repeated. The Sloan $i$ filter, which we are using at the Swope telescope for the low redshift part of the CSP, overlaps well with the $Y$-band for a redshift of z$\sim$0.35, and the $J$-band at redshift z$\sim$0.63 (see Figure 2). If targets at these redshifts were available, they moved to the top of our observing priority list. We aimed to obtain Magellan observations no more than a few days after maximum light, and preferably while still on the rise. Our criteria for selection of the SNLS, ESSENCE and SDSS-II objects were: 1) the SNe Ia were in the redshift range $0.2 < z < 0.7$, 2) the SN Ia was estimated to be near maximum, 3) SNe Ia near $z = 0.35$ and $z = 0.65$ were given preference and 4) preference was given to SNe Ia well-separated from the host. In practice, criteria 3) and 4) were rarely invoked since there was not much choice after criteria 1) and 2). Our selection criteria therefore matched fairly closely those of the parent surveys.

The SNLS, ESSENCE and SDSS-II projects provided coordinates, finder charts and epochs of high-probability SN Ia candidates for the Magellan observations. In three cases (SNLS 03D1gl, SNLS 04D2cw, ESSENCE 2004-H-280), the spectral classifications were later revised (to types other than SNe Ia). In one case (SNLS 04D2al), the redshift was too large ($z = 0.838$) and the SN Ia was undetectable in our observations. In Table 2, we list the SN Ia name, position, number of CSP observations, and IAU cross-identification, for the SNe Ia.

## 3. INSTRUMENTATION AND OBSERVATIONS

### 3.1. *Instrumentation*

Our NIR imaging has been carried out using $Y$- and $J$-band filters on the Persson Auxiliary Nasmyth Infrared Camera (PANIC) (Martini et al. 2004). This camera is mounted on the east Nasmyth platform of the Magellan Baade telescope. It contains a 1024x1024 HgCdTe Hawaii-1 array with a scale of 0.125 arcsec pixel$^{-1}$, and covers a field of view of $2.1\,' \times 2.1'$ on the sky.

### 3.2. *Observations*

#### 3.2.1. *Observing Strategy and Current Status*

Our observing goal was to acquire $Y$ and/or $J$ photometry with gaps in the SN Ia light curves no larger than 7 days, straddling the light curve over maximum light if possible. To avoid large gaps, PANIC was scheduled during dark/grey time, in addition to the customary bright time for infrared instruments. In practice, telescope time was scheduled with gaps generally less than 5 days, although gaps of 8 days were occasionally unavoidable. A record of observations, including finding charts of the objects, is maintained on our web site for the project, which can be found at http://www.ociw.edu/csp/. Generally, 3 to 5 observations per SN Ia were obtained.

We began this long-term project with a pilot program in November 2003 running through April 2004, centered on the best weather period at Las Campanas. Our first host-galaxy images (once the SN Ia had faded) were obtained in the following year. In the second year, we observed from October 2004 through March 2005. Unfortunately, poor weather at Mauna Kea during the northern winters of 2003 and 2004 resulted in a very low yield of SNe Ia for CSP follow-up during this pilot project. Moreover, ESSENCE was operational only during the northern fall, and SDSS-II began routine operations during the fall of 2005. We therefore shifted the CSP follow-up campaigns to August through January when there was good overlap with all three SN search programs.

After four campaigns, we obtained Y and/or J photometry for a total of 80 objects, 75 of which were ultimately confirmed as SNe Ia. Follow-up host-galaxy observations have been obtained for 71 of these SNe Ia and we are in the process of obtaining host-galaxy images for the remaining objects. The redshift distribution for our total sample is shown in Figure 3. In this paper, we report on the photometry from the first 35 SNe Ia. A summary of the observations for these 35 SNe Ia is given in Table 2. At the current time, data for 20, 13, and 2 SNe Ia have been analyzed from the SNLS, SDSS-II and ESSENCE surveys, respectively. The original goal of the CSP was to acquire a sample of 100 objects over the redshift range $0.1 < z < 0.7$; however, with the conclusion of the three surveys, our expected sample will be limited to 75 SNe Ia.

#### 3.2.2. *Observing Procedures*

Twilight sky flats were taken in each filter every night in at least 5 dithered positions with 2 exposures at each position, controlling the count level to be in the linear regime. The detector becomes nonlinear at the 1% level at approximately 13,000 ADU and at the 5% level at approximately 35,000 ADU. Dark frames were taken in sets of 15, each with exposure times matching those of the science images. The SN Ia observations were obtained using 9 dither positions with 2 exposures per position. The exposure times used for individual images were 120 seconds with total exposure times ranging from 2160 to 8640 sec. Reference images for these SN Ia fields were taken in the same manner once the SN Ia faded, to allow accurate background subtraction. The signal to noise in the stacked reference images were as high (or higher) than those in the SN Ia images, so as not to degrade the photometry. The seeing for these images ranged typically between 0.4 and 0.8 arcsec. On photometric nights, 3 to 5 stars chosen from the standard system defined by Persson et al. (1998) were observed throughout the night in each filter. These standard stars were observed in 5 dither positions with 2 exposures at each position. The exposure times of individual images were 3 or 4 seconds, resulting in total exposure times of 30 and 40 seconds. On occasion, the telescope was de-focused to ensure the counts remained in the linear regime of the detector.

## 4. DATA ANALYSIS

### 4.1. *Pipeline Processing*

We have developed an automated pipeline to process the PANIC images. The pipeline carries out (1) linearity corrections, (2) dark combination and subtraction, (3) bad-pixel mask production, (4) flat-field combination and division, (5) sky image computation and subtraction and (6) combination of dithered frames into final

stacked images. We apply a predetermined linearity correction law to every pixel value above 8,000 ADU. The multiplicative correction ranges from 1.0 at 8000 ADU to 1.06 at 40,000 ADU. Dome flats are created by subtracting images of equal exposure times taken with no dome lamps from those with the dome lamps on. The final dome flats are used only to build bad pixel masks for each night and median-combined twilight sky flats are used for flat-fielding. Sky frames are subtracted from the individual object frames using modal scale factors. Finally, stacked images are created by aligning and averaging the individual object frames.

### 4.2. *Galaxy Template Subtraction*

To obtain accurate photometry for the SNe Ia, the host galaxy light must be subtracted from the images. The strategy for removing the host galaxies from the SN Ia data involves three steps: (1) obtaining host-galaxy images of the SN Ia fields in the year following the events; (2) registering and matching the point-spread functions (PSF) of the images; (3) subtracting the PSF-matched SN Ia and host-galaxy images. The algorithm developed for the registration and non-parametric matching of the PSFs will be described in more detail in a later paper (Kelson et al. 2009); the method is summarized briefly here.

For a given SN Ia image and associated host-galaxy image, SExtractor (Bertin & Arnouts 1996) is used to identify objects down to a threshold of 3-$\sigma$. The positions of these objects are used to compute the coordinate transformation between each SN Ia image and the host-galaxy image. Matching the PSF of the host-galaxy image, $T$, to that of the SN Ia image, $S$, consists of solving for the convolution kernel, $k$, that maps point-sources in $T$ to $S$. Once $k$ is known, the entire host-galaxy image can then be convolved with $k$ and subtracted from $S$ to isolate the SN Ia. However, our fields of view are small and in several instances lack suitable point sources for determining the kernel using more traditional techniques, for example, parameterizing the kernel with a Gaussian (Alard & Lupton 1998, Alard 2000). Instead, we use a non-parametric technique that utilizes all objects in the field to constrain the kernel. The kernel consists of a $(2M+1)\times(2M+1)$ matrix indexed by $u$ and $v$, and is determined by minimizing

$$\chi^2 = \sum_i^N \left| \frac{S\left(x_i, y_i\right) - \sum_u \sum_v k\left(u, v\right)\left[T(x_i - u, y_i - v)\right]}{\sigma(x_i, y_i)} \right|^2 \tag{1}$$

where the sum is over $N$ pixels in the source and template images.

The matrix of $T(x_i - u, y_i - v)$ is decomposed using singular value decomposition, and its constituent eigenvectors contain the kernel's natural set of orthogonal basis functions. The eigenvalues represent each eigenvector's sensitivity to noise. We eliminate those basis functions that do not contribute to reducing the $\chi^2$ per degree of freedom. Because image re-binning is mathematically equivalent to a convolution, errors in the registration are fully accounted for by the convolution kernel that minimizes $\chi^2$.

Ideally, one wishes to convolve (i.e., degrade) the host-galaxy images so as not to decrease the signal-to-noise of the SN Ia. However, approximately 8% of our SN Ia images were taken under exceptional seeing conditions (less than 0.35 arcsec) which, to date, have not been matched in our host-galaxy observations. As a result, this subset the SN Ia images have to be degraded to match the poorer image quality of the host-galaxy images. Fortunately, these SNe Ia have lower redshifts ($z \leq 0.3$) and are relatively bright, so that the signal to noise remains high. The SN Ia images in our sample to date have a range of image quality, from 0.3 arcsec to 1.4 arcsec; the host-galaxy images have a range of image quality, from 0.3 arcsec to 1.3 arcsec. We find that our image subtraction technique works well for removing the host galaxies for a wide range of seeing conditions, position of the SN Ia relative to the host galaxy, and redshift. Three examples of a host-galaxy-subtracted image are shown in Figure 4, for objects at redshifts of 0.25, 0.30, and 0.68, respectively.

### 4.3. *Photometry*

Observing SNe Ia in the NIR is more challenging than in the optical owing to higher sky background. The contrast of SN Ia to galaxy is also less in the red, and overcoming these effects require longer integrations than in the optical. We measure the flux with a two-step approach. The first step is to measure the magnitudes of several stars in each SN Ia field, which we shall refer to as tertiary standards. The primary standards are those that establish the JHK system (Elias et al. 1982), on which the secondary standards (Persson et al. 1998) that we observe are based. In choosing the tertiary standards, we require that: 1) the star is no closer than 20 arcsec to the edge of the PANIC field of view 2) the star appears in all observations of the SN Ia and the host galaxy; and 3) there are no significant residuals for the star after host-galaxy subtraction. We use DAOPHOT and DAOGROW (Stetson 1990) to measure and fit a growth curve (flux versus aperture size) for each star. We then compute an aperture correction using these fits to get the flux measured through a 10-arcsec-diameter aperture, matching the aperture used on the standards. These fluxes are therefore calibrated with respect to the secondary standards observed that evening, and are then averaged over all photometric nights.

The second step is to measure the flux ratios between the SN Ia and the tertiary standards. At the highest redshifts, we are working at the detection limit of the telescope where DAOPHOT and DAOGROW are no longer robust. Instead, we use the optimized extraction algorithm of (Naylor 1996). In brief, the brighter stars in the field are used to estimate the PSF, $P_{i,j}$, modeled as a superposition of Gaussian and Moffat profiles. This estimated PSF is then used as a weight mask in summing the flux from the SN Ia pixels: $F = \sum_{i,j} w_{i,j}\left(D_{i,j} - S_{i,j}\right)$ where $w_{i,j} = \frac{P_{i,j}}{\sum P_{i,j}^2}$, $P$ is the model PSF, $D$ is the measured counts, and $S$ is the sky flux. Following Naylor (1996), we have assumed that the variance in the weights is dominated by the sky ($V_{ij} \simeq V_s$ in his equation (10)). This yields an optimized estimate of the flux for the SN Ia. We then use the same weight mask to measure fluxes and compute flux ratios between the SN Ia and each tertiary standard. These flux ratios, together with the calibrated fluxes from step 1, provide estimates of

the calibrated flux of the SN Ia. These estimates are averaged to yield the final calibrated flux for the SN Ia. We have done a number of tests in which fake point sources are inserted into the frames and then recovered, and find that the method works extremely well. These results will be reported in Kelson et al. (2009).

We have also taken great care in computing the variances of our fluxes. In the process of correcting for image distortion in the PANIC pipeline, rectifying the images, convolving with a kernel, and then subtracting a host galaxy image, the pixels in each image have become correlated. We produce variance maps for each observed field early in the PANIC pipeline. A simple propagation of errors is done at each step of the pipeline, updating the variance in each pixel in the maps. The final variance maps are used to compute the noise rather than image statistics, ensuring that we can properly estimate the variance of the tertiary standards and the SN Ia.

### 4.4. *Absolute Calibration*

The absolute calibration of the Magellan photometry is based on $JHK$ standard stars from Persson et al. (1998), where the zero point is tied to Vega. Currently, we are applying the $Y$-band absolute calibration described in Hamuy et al. (2006), using Kurucz model spectra and Hillenbrand et al. (2002) standard star measurements. Contreras et al. (2009) have recently obtained new observations confirming this calibration to an accuracy of $\pm 0.01$ mag. We have observed common standard stars and adopted the same procedures for the reduction of the standard stars so that differences in the calibration of low- and high-z samples are minimized. Adopting atmospheric extinction coefficients of $k_Y = 0.10$ and $k_J = 0.12$ mag/airmass following Hamuy et al., we solve for the nightly zero points in each filter. Photometry for the standard stars is obtained with apertures of diameter 10 arcsec. The statistical errors in the zero point are determined from the scatter of individual measurements and range from $\pm$ 0.01 to $\pm$ 0.05 mag. A minimum of three photometric nights determines the absolute flux for each SN Ia (see §4.3). The average scatter in the zero points based on observations of standard stars is 0.023 mag at $J$ and 0.013 mag at $Y$.

In this (and other CSP) papers, we are presenting our photometry in our own natural system. The advantage of using the natural system is that it avoids the uncertainties resulting from the broad features present in the spectra of SNe Ia, which present challenges for the transformation onto the standard system. As outlined in Contreras et al. (2009), the natural photometry is obtained by first computing color terms that transform local standard sequences of stars to the system appropriate for each filter (Landolt (1992) standards for $BV$, Smith et al. (2002) standards for $ugri$, and Persson et al. (1998) for $YJ$). These color terms are then used in reverse to transform the standard magnitudes to our natural system and it is these magnitudes that are used to calibrate the SN Ia photometry. The natural magnitudes are therefore equal to the standard magnitudes at zero color. Our natural system magnitudes can be straightforwardly transformed to other systems. Transmission curves for our NIR and optical filters are given in Hamuy et al. (2006) and Contreras et al. (2009), and updated versions are available online at the CSP web site. In the SN Ia target fields, we identified several isolated stars to serve as tertiary standards to determine absolute flux for those nights that were not photometric. Photometry for these secondary standards is also available on line. In Table 1, we list the filters, effective wavelengths, and published references to the calibrations relevant for the CSP. A comparison of our own NIR $YJ$ photometry (K-corrected to the $i$ band) to that of the optical surveys (SNLS, ESSENCE and SDSS-II) requires that we adopt a standard with a measured spectral energy distribution (SED) spanning the optical and NIR. For this purpose, we have chosen the Bohlin & Gilliland (2004) model for Vega, as updated in Bohlin (2007).

## 5. SYSTEMATIC EFFECTS

As the number of objects has increased, SN Ia cosmology has reached the stage where the systematic uncertainties are becoming the dominant source of error. The CSP has been designed to minimize known systematic effects, particularly those due to K-corrections, reddening, and cross calibrations to different photometric systems. Below we discuss our current approach to dealing with K-corrections and reddening.

### 5.1. *K-corrections*

The observed SEDs of SNe Ia are shifted and stretched with redshift due to the expansion of the Universe. Accurate corrections for these effects (K-corrections) for SNe Ia remain an observational challenge, and much effort has been put into creating libraries of SN Ia spectra with which to assemble SEDs that can be used to estimate the K-corrections and their variance (Nugent et al. 2002; Hsiao et al. 2007). The K-corrections are computed in a manner similar to Kim et al. (1996) and Nugent et al. (2002), using the following formula:

$$K_{AB}(t) = 2.5\log(1+z) + 2.5\log\left[\frac{\int R_B(\lambda)\,\Phi'(\lambda;t)\,\lambda d\lambda}{\int R_A(\lambda)\,\Phi'(\lambda(1+z);t)\,\lambda d\lambda}\right] + \mathcal{Z}_A - \mathcal{Z}_B \quad (2)$$

where $A$ represents the observed filter and $B$ represents the rest-frame filter to which we are transforming, $R_A$ and $R_B$ are the corresponding observed and rest-frame filter response curves, and $\mathcal{Z}_A$ and $\mathcal{Z}_B$ are the photometric zero-points. The K-corrections are therefore applied in the following sense: $m_B = m_A - K_{AB}$. The spectral energy distribution (SED) $\Phi'(\lambda;t)$ at epoch $t$ is obtained by "color-matching" the corresponding SED template from Hsiao et al. (2007). Initially, K-corrections are computed using unmodified Hsiao et al. (2007) SED templates and applied to the photometry. Light-curve templates are then fit to the $N$ filters for which there is optical and NIR photometry yielding $N-1$ colors as a function of epoch. We then construct a smooth function $S(\lambda)$ which, when multiplied by the template SEDs, yield synthetic colors equal to the observed colors; i.e., we model the template rather than the (more noisy) observed colors. Finally, these improved SEDs are used in Equation 3 to compute the final K-corrections. This color-matching simultaneously accounts for the intrinsic color variations from SN Ia to SN Ia as well as reddening corrections due to dust.

Hsiao et al. (2007) demonstrate that while K-corrections are determined mainly by broad-band colors,

accounting for differences in spectral features is also necessary. These corrections are based on a larger library of spectra, with a greater number of epochs and wavelength coverage than previously available. They include 67 spectra from the CSP (34 of which cover the I-band), obtained at the DuPont telescope, and made available to Hsiao et al. for this purpose. Overall, this new library contains many more spectra with red wavelength coverage, and the telluric features at $\lambda \simeq 6880$Å, 7200Å, 8200Å, and 9400Å have been identified and removed. In the $I$-band, the Hsiao et al. template includes approximately 250 spectra. Determining accurate K-corrections in the $i$-band requires careful attention to the broad Ca II triplet P-Cygni absorption feature (8498, 8542 and 8662Å). Fortunately, for the purposes of the CSP, it is only well after maximum light has occurred that the Ca II feature changes dramatically (Hsiao et al. 2007, see Figure 5). Currently, in the spectral region of the $i$-band, 125 spectra have been used for the K-correction template. We are continuing to acquire additional spectroscopy of our low-redshift candidates, specifically to improve the K-corrections as a function of both epoch and decline rate of the SNe Ia.

We show in Figure 5 typical cross-band $K_{iY}$ and $K_{iJ}$ corrections based on the Hsiao et al. (2007) library, plotted as a function of time since maximum light at $B$, for redshifts 0.2, 0.3, 0.45, and 0.6. For comparison, we also show the K-corrections from Nugent et al. (2002). Given the currently larger number of available $I$-band spectra, and correction for the presence of telluric features, we have adopted the newer K-corrections from Hsaio et al. for the purposes of this study. The greatest differences occur at early times, 10 days before peak magnitude. The corrections are greatest at late times in the SN Ia evolution, as well as very early times for z=0.6. For our observations around peak magnitude, the K-corrections at these redshifts range from $-0.5$ to $-0.3$ magnitudes in Y-band and from $-1.1$ to $-0.9$ magnitudes in J-band. Table 3 contains our currently adopted values for the $K_{iY}$ and $K_{iJ}$ -corrections. In order to estimate the uncertainties in the K-corrections, we apply the same procedure to the SNe Ia whose spectra were used to generate the template SEDs themselves. For those epochs with spectra, we can compute the K-corrections using the color-matched SED and the observed library spectrum, and compare the results. For each redshift, we compute synthetic photometry and K-corrections based on the library spectrum and appropriately redshifted filter functions, simulating what would be observed if this SN Ia were at redshift $z$. The SED template is then color-matched to these synthetic observed colors and the K-correction computed again. This is repeated for each library spectrum and the *rms* difference between the library and template K-corrections is computed. Since ESSENCE, SNLS, and SDSS-II have three different filter sets, we have separately computed the uncertainties in each case.

In Figure 6 we plot the statistical dispersion in the K-corrections as a function of redshift for the filters used in ESSENCE, SDSS-II and SNLS. The dispersion is sensitive to the filter set used, which determines the accuracy with which we can color-correct the template SED. As expected, the dispersions are lowest at the redshifts where the observed and rest-frame filters overlap and increase at higher and lower redshifts. The largest uncertainties arise when there are no filters to anchor the blue side of the SED at low redshifts or, alternatively, the red side at high redshifts. For comparison, we plot the dispersions with (solid) and without (dashed) including the NIR photometry; in most cases, the curves overlap and are indistinguishable. In general the statistical uncertainties in the K-corrections range from $\pm 0.005$ to $\pm 0.05$ mag. The largest uncertainty is for d149 at a redshift of 0.34, where the transformation to the $B$-band reaches an uncertainty of $\pm 0.1$. Similarly, for four SDSS objects at z<0.25 (SN 3331, 5549, 7243, and 7512), the uncertainties also reach $\pm 0.1$ mag. For the SNLS objects, the statistical uncertainties in the K-corrections are generally less than $\pm 0.04$ mag. The errors for individual epochs for a given object are correlated, and a combined, weighted uncertainty is applied to the distance modulus (or peak magnitude). These uncertainties are included in the total statistical uncertainties computed for each individual SN Ia. We carry these uncertainties in the analysis of cosmological parameters described throughout this paper. Fortunately, progress is continuing to be made in improving K-corrections for SNe Ia. The spectral library will continue to grow in the next few years with additional spectra from numerous groups, including the low-redshift CSP.

### 5.2. *Extinction Corrections*

Correcting accurately for extinction remains a challenge for SN Ia cosmology. The issue is complicated by many factors:

1) there are at least four separate potential sources of dust: a) foreground (Milky Way Galaxy) dust, b) dust within the host galaxy, c) dust associated with the circumstellar material of the SN progenitor and d) dust in the intergalactic medium.

2) there is no *a priori* knowledge of the dust properties in the latter three of these environments and the reddening laws could, in principle, be different in all three environments, perhaps being a function of metallicity, atmospheric environment of the SN Ia, or even evolving as a function of time.

3) even if the extinction law(s) is known perfectly, correcting for reddening requires knowledge of the intrinsic colors (and their dispersion) to derive a reddening curve. The observed color of a SN Ia is determined by the intrinsic SED of the SN Ia, reddening due to dust, and the expansion of the Universe (the K-correction). Hence, there is an inherent circularity in the problem, and generally some assumptions are made (e.g., that the intrinsic colors of SNe Ia are known, and that they are known as a function of redshift and environment, and/or that the reddening law is universal). At present, for SNe Ia, it is still not possible to distinguish unambiguously between a different reddening law and differing intrinsic colors.

The reddening law can be characterized by a ratio of total-to-selective absorption, $R_\lambda$, which generally increases toward shorter wavelengths: $R_\lambda = A_\lambda/E(B-V)$, where $A_\lambda$ is the total absorption at each wavelength, $\lambda$. On average, the ratio of total-to-selective absorption, $R_\lambda$ decreases from 4.9 at $U$, to 4.1 at $B$, 3.1 at $V$ and 1.7 for the $I$-band in the Galaxy (e.g., Cardelli et al. 1989). For a reddening of, say, $E(B-V) = 0.02$ mag, the corrections to the rest-frame $U$-band magnitude would be

$\sim$0.10 mag and $\sim$0.03 mag at $I$. Thus, longer-wavelength observations offer a significant advantage in minimizing systematic effects due to reddening.

In general, it has been concluded that the dust properties in other host galaxies appear to be similar to those in the Milky Way (see, for example Riess et al. 1996; Phillips et al. 1999; Knop et al. 2003; Riess et al. 2004; Jha et al. 2007). To date, no empirical evidence for grey dust has been found (e.g., Knop et al. 2003; Riess et al. 2004, 2007); i.e., larger dust grains with wavelength-neutral effects. However, some studies have indicated that the reddening law for SNe Ia is consistent with $R_V \sim 2.5$, lower than the Galactic reddening law (e.g., Wang et al. 2006). Correcting for SN Ia reddening has generally made use of one or more of the following approaches: 1) using a sample of SNe Ia where the reddening is expected to be negligible in order to define a zero-extinction fiducial sample (e.g., SNe Ia in elliptical galaxies: Hamuy et al. 1996c; Phillips et al. 1999) and/or 2) making use of a discovery by Lira (1995) that after $\sim$30 days, the $(B-V)$ colors of SNe Ia show a very small dispersion (e.g., Phillips et al. 1999; Prieto et al. 2006; Jha et al. 2007), or 3) not correcting directly for reddening, but solving for a general $(B-V)$ color term that treats the differences in SN Ia intrinsic colors and reddening as indistinguishable (e.g., Tripp 1998; Astier et al. 2006).

We have dealt with the extinction using two different methods. First, we use a "reddening-free" magnitude, as described below. For comparison, we also have solved for the reddening explicitly following Phillips et al. (1999), in which an intrinsic color is assumed for a given value of $\Delta m_{15}$ and the observed color (after K-corrections and Milky-Way reddening corrections are applied) yield the reddening due to the host galaxy. We differ from Phillips et. al in that we allow for negative reddenings in the models. While a negative reddening is not *physical*, measuring a negative value for the reddening parameter is certainly statistically possible given the uncertainties in the measured photometry, and our uncertainty in the intrinsic dispersion of SN Ia colors. For the whole sample of SNe Ia, the results are statistically unbiased. We list the reddenings, corrected for Galactic foreground reddening, for our individual SNe Ia in Table 5. The mean reddening for the low redshift sample is $< E(B-V) > = 0.06$ with a standard deviation of 0.09, consistent with that for the high redshift sample, with $< E(B-V) > = 0.05$ and a standard deviation of 0.10.

We proceed to compute a reddening-free magnitude, $w$ (Madore 1982; Freedman et al. 2001), defined here as:

$$w^i_{BV} = i - R^i_{BV}(B-V) = i_0 - R^i_{BV}(B-V)_0 \qquad (3)$$

where the subscript, 0, refers to intrinsic (unreddened) magnitudes and magnitudes without subscripts are observed magnitudes. The reddening coefficient $R^A_{BC}$ is defined as

$$R^A_{BC} \equiv \frac{A_A}{E(B-C)} = \frac{R_A}{R_B - R_C}$$

where $R^I_{BV} = 1.9$ and $R^I_{BI} = 0.8$ for the case of a standard reddening law (with $R_V = 3.1$), while $R^I_{BV} = 1.1$ and $R^I_{BI} = 0.5$ for $R_V = 2.0$(Cardelli et al. 1989). The advantage of reddening-free magnitudes is that no knowledge of either the intrinsic colors of SNe Ia, nor a sample of unreddened SNe Ia is needed: $w^i_{BV}$ is defined such that the observed and intrinsic combinations of these magnitudes and colors are numerically equivalent. This method is in wide use for Cepheid variables. However, (just as for other methods), the same color coefficient is applied to both the nearby and distant samples. It should be noted that this is equivalent to using the color term, $\beta$, of Astier et al. (2006) if the fiducial color of a SN Ia is 0. Indeed, it would simply be a reddening correction if all SNe Ia had zero colors. An advantage of this method is in the case where the reddening is solely due to dust extinction when this approach will correct for it without the need to isolate an unreddened sample. Furthermore, the $\beta$ coefficient used by other authors will be the reddening coefficient in such a case.

Given the definition of $w^i_{BV}$, and because we are adopting a single reddening coefficient, it makes no difference to the final results whether we deal with reddening-free magnitudes or reddening-corrected magnitudes; the results are mathematically equivalent. For both methods, we used the high- and low-redshift data to determine the best value of $R_V$ by minimizing the scatter in the Hubble diagram, while simultaneously solving for the best-fit cosmology.

### 5.3. *Other Systematic Uncertainties: Evolution, Metallicity and Weak Lensing*

In addition to the uncertainties in K-corrections and extinction discussed above, there are other potential uncertainties on the luminosities of SNe Ia (e.g., evolution, metallicity, and weak lensing). For completeness we briefly summarize the observational situation with respect to these effects. It is observed that spiral galaxies host slower decliners, and hence, more luminous SNe Ia (Hamuy et al. 1996c; Riess et al. 1998). In general brighter SNe Ia occur in bluer, lower-luminosity galaxies (Hamuy et al. 2000). In addition, the scatter in the Hubble diagram is observed to be a function of morphological type of the host galaxy (Sullivan et al. 2003). Gallagher et al. (2008) have noted a correlation for nearby E/S0 galaxies such that SNe Ia in older galaxies are fainter than those in galaxies with younger global ages, as estimated from stellar population models. Further, they find that residuals in the Hubble diagram correlate with the host-galaxy metallicity. Constraints on differing individual SN Ia properties are now coming from detailed comparisons of SN Ia spectra (Hook et al. 2005; Balland et al. 2006; Blondin et al. 2006; Riess et al. 2007). To date, these studies have revealed no evidence for significant evolution or metallicity differences. However, there appear to be systematic differences at shorter wavelengths, particularly in the restframe ultraviolet (Ellis et al. 2008; Foley et al. 2008). Although empirically such effects appear to be small relative to the cosmological effect being measured (e.g., Hamuy et al. 1995; Riess et al. 2004; Knop et al. 2003; Astier et al. 2006), understanding at what level these factors affect the observed properties of SNe Ia is critical to SNe Ia cosmology. We will return to these questions as more data become available and we complete the CSP. Finally, we note that the net magnification due to weak lensing is not predicted to be significant

at redshifts z<0.7 (Holz 1998), the redshift interval of the CSP sample.

## 6. LIGHT CURVES AND DECLINE RATES

In Figures 7 to 10, we present optical and $YJ$-band light curves for the 35 SNe Ia with host galaxy subtractions. The $YJ$-band data and uncertainties are given in Table 3. We also show the optical light-curve data from the SNLS, ESSENCE, and SDSS-II surveys. The solid lines are template light curves, generated as described below. The quality of the light curves in general is quite good, and there is an excellent correspondence between the optical and the NIR data. For the CSP photometry, the average $Y$-band uncertainties are ±0.03 mag, ±0.06 mag (±0.10 mag at $J$), rising to ±0.08 mag (±0.19 mag at $J$) for the redshift intervals $0.1 < z < 0.3$; $0.3 < z < 0.5$; and $0.5 < z < 0.7$, respectively.

We make use of our own CSP low-redshift, optical data (Contreras et al. 2009; Folatelli et al. 2009) for comparison with our NIR sample at higher redshifts. The low-redshift sample is currently comprised of 21 well-observed SNe Ia (those labeled Best Observed in Table 1 of Folatelli et al. (2009)), with redshifts $z > 0.01$, and with $E(B-V) < 0.5$ mag. As described in more detail in Burns et al. (2009), we construct a set of $BVgri$ light-curve templates based on this sample of 21 CSP SNe Ia. We use a technique similar to that of Prieto et al. (2006) to generate the light-curve templates shown in Figures 7 to 10, and determine the $\Delta m_{15}$ decline-rate values and time of $B$ maximum using $\chi^2$ minimization. The fits are done in flux space simultaneously for the optical and NIR data. This technique will be refined as additional data are obtained during the low-redshift part of the CSP. As shown in Figure 1, the $i$-band light curves usually exhibit a second maximum, which can vary in strength from event to event. The variations of the $i$-band template are included in the error budget when fitting the $i$-band templates; these become a statistical error when the $i$-band distance moduli are plotted in the Hubble diagram. As described in §5.1, K-corrections were computed by first color-matching the SED from Hsiao et al. (2007) to the light curves at each epoch. Independent co-authors (CB, GF, and MP) performed a double-blind check of the light-curve parameters ($\Delta m_{15}$), the K-corrections and the reddenings. Our derived light-curve parameters are given in Table 5. As discussed earlier, some of the derived $E(B-V)$ values have negative values. Given the measurement uncertainties and color fluctuations of ±0.06 mag, however, these negative values are not significant.

## 7. A COMPARISON OF PROPERTIES OF THE CSP LOW- AND HIGH-REDSHIFT SNE IA

We compare here the restframe $(B-V)$ and $(V-i)$ colors for the CSP nearby and high-redshift samples analyzed in this paper. These colors are computed based on the peak magnitudes in each band. In Figures 11 and 12 we show histograms for the 21 nearby SNe Ia ($z < 0.1$) and 35 more distant CSP SNe Ia with ($0.12 < z < 0.70$). The mean colors and 1-$\sigma$ dispersions for our sample are $(V-i)$ = -0.63 ± 0.12 mag and $(V-i)$ = -0.67 ± 0.16 mag at low and high redshifts, respectively. For $(B-V)$, the mean colors are $(B-V) = 0.04 \pm 0.09$ mag and $(B-V) = 0.02 \pm 0.10$ mag, respectively. The colors are consistent to within the uncertainties. However, the very red CSP objects SN 2005A and SN 2006X have not been included in this analysis since they do not fit our redshift or reddening criteria, as defined above. In Figure 13 we show a comparison of the distribution of values for $\Delta m_{15}$ for the low- and high-redshift samples. The mean values for $\Delta m_{15}$ are 1.11 ± 0.28 and 1.18 ± 0.33 for the nearby and more distant samples, respectively. There is good overlap in the two distributions, although the distant sample is more peaked. Given the different selection effects for the different samples and the possibility of SN Ia evolution, we do not necessarily expect the low- and high-redshift distributions to agree. For this small sample, quantitative comparison is limited; however, we conclude that the low-redshift sample spans the parameter space of high-redshift color and $\Delta m_{15}$.

## 8. DISTANCE MODULI, REDDENINGS AND ERRORS

We now turn to the determination of the distance moduli, reddenings and the errors associated with these quantities. We undertake a simultaneous fit for the distance modulus as well as three parameters used to define the absolute magnitudes. We include both the low- and high-z SNe Ia in this analysis. For each independent choice of three filters used to define the reddening-free magnitude (generally $BVi$), we use the following three parameters to define the absolute luminosity of a SN Ia. We treat these three quantities as nuisance parameters in this analysis.
1) $W_0$, the absolute reddening-free magnitude of a SN Ia with $\Delta m_{15} = 1.1$
2) $b$, the slope of the $W$-$\Delta m_{15}$relation and
3) $R_V$, the ratio of total-to-selective absorption.
The absolute (reddening-free) magnitude for a SN is then $W^i_{BV} = W_0 + b\,(\Delta m_{15} - 1.1)$. To compute the distance moduli for the entire sample, we then measure an apparent reddening-free magnitude at maximum light, $w^i_{BV}\,(t_{max})$, for the restframe $BVi$ photometric bands. The distance modulus is then, by definition, $\mu_0 = w^i_{BV} - W^i_{BV}$. Distance moduli are listed in Table 5. (Here, a value of $H_0 = 72$ km/sec/Mpc is adopted. However, the value of $H_0$ cancels out for the determination of other cosmological parameters in §9.)

Using a reduced $\chi^2$= 1 approach (Tremaine et al. 2002), we then compute $\chi^2$ by comparing the measured distance modulus, $\mu_0$, with a theoretical distance modulus $\mu_T\,(\mathcal{C})$ where $\mathcal{C}$ represents the set of cosmological parameters (e.g., $\Omega_m, \Omega_{DE}, w$) we consider:

$$\chi^2 = \sum_j \frac{\left[\mu_j - \mu_T\,(\mathcal{C}, z_j)\right]^2}{\sigma_j^2 + \sigma_{SN}^2} \tag{4}$$

where $\sigma_{SN}$ is the intrinsic dispersion of SNe Ia, chosen such that reduced-$\chi^2 = 1$ (for which we find a value of $\sigma_{SN} = 0.09$), and $\sigma_j^2$ is the total variance for observation $j$ and is given by

$$\begin{aligned}\sigma_j^2 = &\sigma^2(i_{max}) + R^{i2}_{BV}\sigma^2(B_{max} - V_{max}) + b^2\sigma^2(\Delta m_{15}) \\ &-2R^i_{BV}\sigma(i_{max}, B_{max} - V_{max}) - 2b\sigma(i_{max}, \Delta m_{15}) \\ &+2R^i_{BV}b\sigma(B_{max} - V_{max}, \Delta m_{15})\end{aligned} \tag{5}$$

where $\sigma^2(x)$ is the variance in parameter $x$ and $\sigma(x, y)$ is the covariance between parameters $x$ and $y$. A peculiar velocity term of ±300 km/sec is also included. By

minimizing this $\chi^2$ (i.e., the residuals in the Hubble diagram), we simultaneously determine the cosmology and the three nuisance parameters $W_0$, $b$, and $R_V$. In this sense, our method is similar conceptually to that described by Tripp & Branch (1999); Astier et al. (2006); Conley et al. (2008). We defer a discussion of the results for cosmology until §9, and discuss first the results for the decline-rate and reddening parameters from this method.

Using the $i$-band data at maximum, corrected for reddening based on the $BV$ photometry, the results for $W^i_{BV}$ are $W_0 = -18.45 \pm 0.05$ (statistical) $\pm 0.01$ (systematic), $b = 0.38 \pm 0.08$ (statistical) $\pm 0.01$ (systematic), and $R_V = 1.74 \pm 0.27$ (statistical) $\pm 0.1$ (systematic).[26] Since we have data for three filters, we can independently correct for reddening using different combinations of bandpasses (e.g., $B-V$, $V-i$, or $B-i$). However, we prefer to solve for the reddening using simultaneous data from a single photometric/telescope system ($B-V$), which is available for all of the SNe Ia, rather than a hybrid optical-NIR combination. If instead we use the $B$-band data and correct for reddening based on the $BV$ photometry, $W^B_{BV}$, we find $W_0 = -19.11 \pm 0.07$, $b = 0.65 \pm 0.13$, and $R_V = 1.66 \pm 0.27$. Encouragingly, $R_V$ is consistent for the two filter combinations. The final results for the cosmology are consistent to within the uncertainties, with all combinations of bandpasses.

A value of $R_V = 1.74$ is significantly lower than a Milky-Way value of $R_V = 3.1$. A lower value of $R_V$ is also found by Tripp (1998), Tripp & Branch (1999), and Wang et al. (2006). Conley et al. (2008) and Astier et al. (2006) would find an even lower value than ours, consistent with $R_V$ $(= R_B - 1) \sim 1$ (their $\beta = 2$ would correspond to $R_B$), if their color term was associated with the extinction law.

As a check on our reddening corrections, two independent analysis methods were used by two of this paper's co-authors (CB and GF) to determine the nuisance parameters: the reddening-free method outlined above, and the extinction method outlined in Phillips et al. (1999). We initially discovered a large discrepancy between the two derived values of $R_V$. The reason for this discrepancy can be understood from equations 4 and 5. The denominator of $\chi^2$ includes terms that depend on both $R_V$ and $b$. Depending on the magnitude of the variances and covariances, these terms have leverage on the final solution. We have found that a significant issue affecting the derived reddening law is what is assumed for the variance in SNe Ia colors, $\sigma^2(B-V)$, with the value of $R_V$ increasing with increasing $\sigma^2(B-V)$ (see Appendix A). The two analysis methods agree well if consistent errors are adopted. It should therefore be stressed that accurate estimates of the variances in the data are crucial for the determination of $R_V$. As a further test of these different approaches, Burns et al. (2009) have begun to explore this issue with an unbiased estimator using a Monte Carlo Markov Chain (MCMC). This work goes beyond the scope of the present paper, but we note that the preliminary results agree well with those presented here, with $R_V = 1.8$. Our current analysis and that of Folatelli et al. (2009) are consistent with a picture in which, in addition to corrections for Milky-Way-like dust, there is an intrinsic dispersion in the colors of SNe Ia that is correlated with luminosity, but not the decline rate.

Before concluding this section, it is worth emphasizing that disentangling a possible additional intrinsic color term from extinction leaves open a challenge to SN Ia cosmology. Potential differences in either the intrinsic or observed sample populations of SNe Ia with redshift and/or environment, or differences in the reddening law may limit the ultimate accuracy for cosmology, and for reaching systematic uncertainties significantly below the $\sim \pm 10\%$ level. Having highlighted the remaining challenges, we note, however, that the level of the effect we are discussing amounts to less than $\pm 10\%$, and reaching a systematic uncertainty at this level for SNe Ia is already excellent progress. Few other methods in use for dark energy measurements currently offer this kind of accuracy. We now turn to a discussion of the Hubble diagram, and then to implications of different values of $R_V$ on the cosmology.

## 9. HUBBLE DIAGRAM AND COSMOLOGICAL RESULTS

### 9.1. *The First I-band Hubble Diagram for z > 0.1*

In Figure 14, we show the $i$ and $B$-band Hubble diagrams, uncorrected for reddening. The residuals about the best-fit to these data are shown in the panels below. We can immediately see the advantage of observing SNe Ia at red wavelengths relative to the optical. The *rms* dispersions in these plots amount to $\pm 0.17$ and $\pm 0.29$ mag, respectively.

In Figure 15, we present the first $i$-band Hubble diagram for the CSP sample of 35 SNe Ia based on Magellan data (solid blue squares) using the reddening-free magnitude technique described in §6, adopting a value of $R_V = 1.74 \pm 0.27$. The error bars shown in the lower panel represent the formal 1-$\sigma$ uncertainties in the distance modulus and include the combined errors in the photometry, the dispersion in the light-curve templates, the estimated dispersion in K-corrections, the error in the foreground Galactic reddening, and the co-variances between the light-curve parameters. We also include a peculiar-velocity component of $\pm 300$ km/sec. The top curve corresponds to an $\Omega_m = 0.27$ , $\Omega_{DE} = 0.73$ cosmology. For comparison, the small black squares indicate distance moduli from Astier et al. (2006). The current CSP sample of 21 nearby SNe Ia from Folatelli et al. (2009) (solid red circles) is also shown in Figure 15. The low-redshift sample is restricted to nearby SNe Ia in the Hubble flow, having redshifts greater than z > 0.010, so that the scatter due to random peculiar velocities is minimized. (The results remain consistent, to within the quoted uncertainties, if we further restrict the sample to z > 0.015 or z > 0.02.)

The immediate conclusion we can draw from this Hubble diagram is that the CSP data alone provide independent evidence for a (standard) cosmological model with $\Omega_m = 0.3$ and $\Omega_{DE} = 0.7$. The CSP constraints can be further improved by combining them with other independent measurements, for example, baryonic acoustic oscillations (e.g., Eisenstein et al. 2005). A weighted fit to our 35 data points in combination with baryon acoustic oscillations (assuming $w = -1$) yields the solution: $\Omega_m = 0.27 \pm 0.02$ (statistical), $\Omega_{DE} = 0.76 \pm 0.13$ (statistical) $\pm 0.09$ (systematic). The systematic

[26] Unless otherwise noted, all reported uncertainties are statistical and correspond to 1-$\sigma$ errors (68% confidence).

uncertainties for SNe Ia do not have much impact on the determination of $\Omega_m$ since this parameter is determined largely by the matter power spectrum. We quote only statistical uncertainties for $\Omega_m$ here. The statistical uncertainties are determined by marginalizing over all other parameters and fitting the 1D probability distribution to a Gaussian. The systematic uncertainties are treated below in §9.3.

Based on the fit to the Hubble diagram above, we show, in Figure 16, our error ellipses in the $\Omega_m$-$\Omega_{DE}$ plane. Consistent with previous SN Ia studies, we find that based on the SN Ia data alone (and the assumption that $w = -1$), a value of $\Omega_{DE} > 0$ is required at greater than the 99% confidence level.

As an alternative to making assumptions about $w$, we can use the CSP data to calculate $w$ under the assumption of flatness ($\Omega_k = 0$). Here we again combine the CSP results with independent measurements of baryonic acoustic oscillations (e.g., Eisenstein et al. 2005), as shown in Figure 17. Assuming a flat cosmology, these joint constraints yield a value of $\Omega_m = 0.27 \pm 0.03$ (statistical) and $w = -1.05 \pm 0.13$ (statistical) $\pm$ 0.09 (systematic). For the purposes of this calculation, we are assuming that $w$ is a constant (i.e., $w_a = 0$). These results are in excellent agreement with other joint constraints from SN Ia studies and baryon acoustic oscillations (Astier et al. 2006; Wood-Vasey et al. 2007; Riess et al. 2007), which also yield values of $w = -1$ and $\Omega_m = 0.3$, to within the quoted measurement uncertainties. We have also combined our CSP results with the two-dimensional probability contours from the 2dF galaxy redshift survey (Hawkins et al. 2003). We find $\Omega_m$ = 0.27 $\pm$ 0.09 (statistical) and $w_0$ = -1.03 $\pm$ 0.23 (statistical), in good agreement with the SDSS data, but with larger uncertainties on the value of $w_0$.

In Figure 18, we show a comparison of the residuals in the Hubble diagram for the high-z data ($z > 0.10$) for the $i$- and $B$-bands relative to the best-fit flat, constant $w$ cosmological model, again for a value of $R_V = 1.74$. The *rms* scatter in the $i$-band Hubble diagram amounts to $\pm$0.13 mag about the fit ; the $B$-band scatter amounts to $\pm$0.15 mag.[27] The resulting cosmological parameters are in good agreement, with differences in $w$ and $\Omega_m$ amounting to only 0.03 and 0.01, respectively, well within the measurement uncertainties. The $i$-band measurements have smaller systematic uncertainties due to smaller reddening corrections, and also have somewhat smaller observed scatter.

As discussed in §6, we find that the smallest scatter in the Hubble diagram at low (as well as high) redshift is found for a value of the (color coefficient or) ratio of total-to-selective absorption $R_V = 1.74 \pm 0.27$. The standard Galactic reddening law is $R_V = 3.1$. In Table 7, we show the fits to $\Omega_m$ and $\Omega_{DE}$ and the *rms* scatter about the cosmological fit for two values of $R_V$, 1.74 and 3.1, for both the $i$ and $B$-band data. For an adopted value of $R_V = 1.74$, the resulting values of $\Omega_m$ and $w$ are in excellent agreement between both bands. However, adopting instead a value $R_V = 3.1$ results in a value of $w = -1.20 \pm 0.13$ for the $i$ data and $w = -1.24 \pm 0.16$ for the $B$ data. The solutions for these different adopted values of the reddening are still mutually consistent, but the scatter in the Hubble diagram increases by about 50% for $R_V = 3.1$. Given the increase in the Hubble diagram scatter at larger redshifts for values of $R_V = 3.1$, and the excellent fit to the low redshift CSP sample for $R_V = 1.74$, we conclude that currently the CSP data are consistent with a lower value of a color coefficient and/or reddening law.

It is interesting to ask what happens if reddening effects are ignored altogether. In this case we find (based on the data shown in Figure 14), that for $i$, $\Omega_m$ = 0.29 $\pm$ 0.03 (statistical) and $w_0$ = -0.90 $\pm$ 0.14 (statistical), consistent to within the systematic uncertainties with the results from the reddening-free and reddening-corrected data discussed above. For the $B$-band data, however, $\Omega_m$ = 0.31 $\pm$ 0.03 (statistical), $w_0$ = -0.70 $\pm$ 0.21 (statistical), and the results for the equation of state are much more sensitive to the treatment of reddening. These results illustrate quantitatively the advantage of the $i$ band in minimizing systematic effects for SNe Ia cosmology. We have also shown that the $i$-band can be calibrated as well as the $B$-band; in fact, there is a further advantage to the $i$-band, where the luminosity-$\Delta m_{15}$ relation has a smaller slope.

It is beyond the scope of this paper to ascertain unambiguously the reddening properties for SNe Ia; however, we make the following observations. The simplest assumption, the application of a standard reddening law coefficient, $R_V = 3.1$ alone, does not provide the best fit to either the low redshift or high redshift CSP data as defined by reduced scatter in the Hubble diagram. As noted previously, this in and of itself does not imply a different reddening law within the host galaxies. For example, it could be indicating an intrinsic color term or perhaps an unusual kind of reddening resulting from dust in the vicinity of the SN Ia. In fact, it would be a somewhat unusual circumstance for the dust within the interstellar medium of all SN Ia host galaxies to have different properties from the dust in nearby galaxies; e.g., LMC, SMC and the Milky Way, which are the only galaxies for which the value of $R_V$ can be measured to high accuracy and where on average it is found to be equal to 3.1 (Draine 2003). Nobili and Goobar (2008) have determined the average reddening law for a sample of 80 SNe Ia and find that it agrees with Cardelli et al. (1989) for $R_V$ 1.75 $\pm$ 0.27. It has also recently been shown that normal dust which is distributed locally around the SN can produce a reddening law with lower value of $R_V$ (Goobar 2008). In other words, this abnormally low value of $R_V$ may simply be due to the geometry of local dust around the SN, which dominates any extinction produced by the host galaxy.

We plan a detailed investigation of the reddening law for SNe Ia based on our low redshift CSP sample, which was designed to provide independent determinations of reddening at multiple wavelengths. For the present discussion, we adopt a general color coefficient term consistent with a reddening law (or color term), $R_V = 1.74 \pm 0.27$.

### 9.2. *Dark Energy and Other Parameterizations of the Expansion*

[27] The *rms* values excludes SN 04D2an at a redshift of z = 0.62, which has no reliable rest-frame $V$-band observation and therefore no color correction is possible using only the optical data.

How do we best compare the observational SN Ia data with cosmological models? While a simple question, this issue is non-trivial. As discussed in §1, the expansion of the Universe can be parameterized in terms of the equation of state parameter, $w$. Lacking a physical explanation for the dark energy, this is a helpful parameterization, but it is still just that – a parameterization. It is important to keep in mind what the actual observables are: observations yield magnitudes and redshifts – not accelerations, equations of state or second derivatives of scale factors (the deceleration parameter). In the case of a flat universe, the luminosity distance is given by:

$$d_L(z) = r(z)(1+z) = \int_0^z \frac{z'}{H(z')}, \tag{6}$$

where $r(z)$ is the comoving distance. Because the luminosity distance relates (inversely) to the *integral* of $H(z)$, it does not provide information on how the expansion rate may have changed from higher redshifts to today. A model is required to infer this evolution.

We now turn to a discussion of the equation-of-state parameter, $w$, which is commonly used in current cosmological models. A number of ways to parameterize $w$ have been suggested in the literature (e.g., Linder 2006; Albrecht et al. 2006). The functional forms for the evolution in $w$ have included simple terms that are either linear functions of redshift, $z$ (or scale factor, $a$), but range also to more exotic functional forms. It must be emphasized that while SN Ia data alone provide a very strong case for a non-zero value for $\Omega_{DE}$ (i.e., an additional component to matter and radiation), SN Ia data *alone* do not provide a sensitive means of constraining either the value of $w$ at the current epoch, or its time evolution.

As discussed in §9.1, under the assumption of flatness ($\Omega_k = 0$), SNe Ia can provide a strong constraint on $w$ when combined with another experiment like baryon acoustic oscillations. Given current evidence, flatness is not an unreasonable assumption; for example, we note that either recent $H_0$ or SNe Ia results, in combination with the WMAP observations, yields $\Omega_k = -0.01 \pm 0.01$ (Spergel et al. 2007). However, additional methods (e.g., baryon acoustic oscillations, cluster growth, weak lensing) must be combined with the SN Ia data to provide meaningful constraints on $w$. At the current time, the accuracy required is not yet sufficient for any of these methods alone, and is the goal of future studies.

The cosmological parameterization $(\Omega_m, \Omega_{DE}, w)$ rests on assumptions about the matter/energy content of the Universe and the functional form for the dark energy equation of state. Here we also investigate another parameterization that is independent of this theoretical framework and involves a purely kinematic model described by the 3 parameters: $(q_0, j_0, \Omega_k)$. Here $q_0 = -\ddot{a}\dot{a}^{-2}a$ is the cosmic deceleration; $j_0 = \dddot{a}\ \dot{a}^{-3}a^2$ is the third derivative of the scale factor, the so-called cosmic jerk; and $\Omega_k$ is the curvature parameter. The only assumption that enters into this parameterization is that the Robertson-Walker metric accurately describes the geometry of the Universe. It is therefore free of assumptions about the energy content of the Universe or even that the Einstein field equations are the correct description of gravity; it is a purely kinematic model. Although currently somewhat out of fashion, it still remains the closest parameterization of the data, since it is acceleration that is actually being measured. In the standard cosmological model $(\Omega_m, \Omega_{DE}, w) = (0.3, 0.7, -1)$, $j = 1$, and $q_0 = -0.67$. As noted by Blandford (2004), lacking an understanding of the dynamics of the Universe, a purely kinematic description remains a well-motivated family of models to explore.

The scale factor is expanded as a Taylor series:

$$\frac{a(t)}{a(t=t_0)} \simeq 1 + H_0(t-t_0) - \frac{1}{2}q_0 H_0^2 (t-t_0)^2 + \frac{1}{6} j_0 H_0^3 (t-t_0)^3 + \ldots \tag{7}$$

from which one can then derive a luminosity distance. Caldwell & Kamionkowski (2004) provide a convenient expansion of the luminosity distance to third order in $z$ and show that to within the precision of this truncation of the Taylor series, the cosmic jerk and curvature can be combined into one parameter ($j_k = j + \Omega_k$):

$$d_L(z) \simeq \frac{cz}{H_0}\left\{1 + \frac{1}{2}(1-q_0)z - \frac{1}{6}\left(1 - q_0 - 3q_0^2 + j_0 + \Omega_k\right)z^2 + \mathcal{O}\left(z^3\right)\right\}.$$

Using the definitions of these parameters and the Friedmann equation, one can derive the transformation equations between the two parameterizations:

$$\begin{aligned} q_0 &= \tfrac{1}{2}\left(\Omega_m + \Omega_{DE}(1+3w)\right) \\ j_0 &= \Omega_m + \tfrac{\Omega_{DE}}{2}\left(2 + 9w(1+w)\right) \\ \Omega_k &= \Omega_m + \Omega_{DE} - 1 \end{aligned} \tag{8}$$

In Figure 19, we show the sum of the jerk and curvature $(j + \Omega_k)$ parameters as a function of $q_0$. A constant value of the jerk is assumed. The grey shading indicates the region where the luminosity distance expansion is valid.[28] The blue contours represent the CSP data using the Caldwell & Kamionkowski (2004) parameterization. The black contours, representing the baryon acoustic oscillation data, were generated using the transformation equations above. The joint constraints from the CSP and baryon acoustic oscillation data yield a value of $j_k = 1.18 \pm 0.44$ (statistical) $\pm 0.27$ (systematic) and $q_o = -0.67 \pm 0.13$ (statistical) $\pm 0.09$ (systematic) at the 95% confidence level. Since jerk and curvature are combined, no assumption of flatness is required. We note that to within the uncertainties, these parameters are consistent with the standard dynamical model with $w = -1$. With future, larger data sets, the discrimination amongst competing models will be sharpened and this type of kinematical prescription will offer a valuable independent test of the current standard cosmology.

### 9.3. *Systematic Uncertainties*

To quantify the effects of systematic errors, we model the effects of known and potential systematic errors for each of the five cosmological parameters discussed in this paper ($w$, $\Omega_m$, $\Omega_{DE}$, $q_0$, and $j_0$). We present in Table 8 the main sources of uncertainty that could contribute to a systematic error, including magnitude and color offsets between the low- and high-redshift samples, errors

[28] Specifically, the error incurred by not including the 4th order term in the Taylor series expansion results in a distance modulus error of $\pm 0.3$ mag at a redshift of 0.7.

in the color terms used to transform the instrumental magnitudes to our natural system, and biases due to the method of $\chi^2$-minimization. We have aimed to give a conservative estimate of the uncertainties. The first column describes the potential source of error and the second column provides a bound on its magnitude. For each of the cosmological parameters, we tabulate the rate of change of the parameter with respect to the systematic (columns 3, 5, 7, 9, 11, 13, and 15) and the resulting error on the parameter (columns 4, 6, 8, 10, 12, 14, and 16). The main sources of potential systematic errors and how we simulate their effects are discussed in more detail in Appendix A.

The final systematic errors adopted are obtained by summing in quadrature the contributions listed in Table 8. From this table, we can see that the current systematic total uncertainty in our measurement of $w$ is $\pm 9\%$. A key element for future SNe Ia studies is improving the absolute calibration of photometric standards (particularly in the era of the Joint Dark Energy Mission, JDEM), ensuring that the calibration minimizes color uncertainties as optical and NIR measurements are compared. Decreasing the uncertainty due to reddening is another critical component of minimizing the overall systematic errors.

Finally, we summarize in Table 9 the values of cosmological parameters from this paper calculated under different sets of assumptions, as described in §9.1, along with both their statistical and systematic uncertainties. When the analysis of our total sample of 75 high-redshift SNe Ia is complete, our statistical and systematic uncertainties will be comparable.

## 10. SUMMARY AND FUTURE MEASUREMENTS

We have used ground-based NIR measurements of SNe Ia to yield an independent Hubble diagram based on *rest-frame* $i$-band data. Reddening effects are a priori lower in the red than the ultraviolet-blue-visual, and we find that $i$-band photometry is an effective tool for mimimizing systematic effects for SNe Ia. Our new observations of 21 SNe Ia at $0.01 < z < 0.08$ and 35 SNe Ia at $0.12 < z < 0.70$, yield the following results:

1) These first CSP data provide independent evidence for an accelerating universe. In the context of a cosmological model including a component of dark energy, $\Omega_{DE} > 0$ at signficantly greater than the 99% confidence level.

2) Joint SN Ia plus baryon acoustic oscillation constraints yield $w = -1.05 \pm 0.13$ (statistical) $\pm$ 0.09 (systematic) and $\Omega_m = 0.27 \pm 0.03$ (statistical) . When the analysis of our total sample of 75 high-redshift SNe Ia is complete, our statistical and systematic uncertainties will be comparable, and at the $\pm 10\%$ level.

3) A purely kinematic solution, with no assumptions about the matter and energy content of the Universe, yields values of $j_k = 1.18 \pm 0.44$ (statistical) $\pm$ 0.27 (systematic) and $q_o = -0.67 \pm 0.13$ (statistical) $\pm$ 0.09 (systematic) for the cosmic jerk and the deceleration parameter, respectively. These results are consistent with an acceleration of the expansion of the Universe, and with the current standard model of cosmology.

4) The current sample of SN Ia photometry is inconsistent with the application of a standard Milky Way reddening law alone, suggesting either that intrinsic color effects dominate the standard reddening corrections, that the SNe Ia are being reddened by dust with different properties than that in the Milky Way, or perhaps there is circumstellar dust about the SN Ia. Future SNe Ia studies will need to disentangle these effect to decrease the systematic errors for SN Ia cosmology.

Beyond a redshift of 0.7, the $i$-band (at restframe 7600Å) is shifted beyond the $1.2\mu m$ J-band in the NIR, rendering $i$-band measurements impossible from the ground. Even before this limit is reached, observations from space are desirable in order to eliminate the bright terrestrial sky background. The CSP data illustrate quantitatively the utility of longer-wavelength data in minimizing systematic uncertainties for SNe Ia cosmology, of relevance for future planned space missions such as the NASA/DOE Joint Dark Energy Mission (JDEM). We suggest that a combination of ground, HST, and future space observations are needed to measure accurately the $i$-band Hubble diagram and constrain the values of $w$ and $w_a$ to the highest possible accuracy.

Finally, we note that while SNe Ia currently provide the most compelling evidence for the acceleration of the Universe, ultimately a combination of different techniques will be required to measure not only $w$, but also its time evolution. Existing degeneracies are such that accurate constraints can be obtained only in the combination of several techniques, or explicitly making the assumption that the Universe is flat ($\Omega_{TOT} = 1$). Future studies of baryon acoustic oscillations, weak lensing, clusters of galaxies, and SNe Ia will yield further complementary and independent estimates of $w$ and $w_a$. SNe Ia will remain a valuable component of future investigations because they naturally cover the redshift range (0.1 to 0.6) where dark energy is measured to be dominant, and cosmic variance is not a major issue for them.

We thank each of the SNLS, ESSENCE and SDSS-II teams for all of their dedicated efforts in discovering SNe Ia, and for providing coordinates and finder charts in a timely manner, allowing the CSP to follow-up these objects. We acknowledge the National Science Foundation (NSF) through grant AST03-06969 for support of the low-redshift component of the CSP and the Department of Energy through grant DE-FG02-07ER41512 for support of the high-redshift CSP. WLF acknowledges the Aspen Center for Physics for its hospitality in June 2007 during the workshop "Supernovae as Cosmological Distance Indicators," as this paper was being written for publication. Funding for the SDSS and SDSS-II has been provided by the Alfred P. Sloan Foundation, the Participating Institutions, the National Science Foundation, the U.S. Department of Energy, the National Aeronautics and Space Administration, the Japanese Monbukagakusho, the Max Planck Society, and the Higher Education Funding Council for England. The SDSS Web Site is http://www.sdss.org/.

## APPENDIX

## SYSTEMATIC ERROR BUDGET

In this appendix, we outline our method for estimating the effects of systematic errors in the determination of various parameters. We have categorized the various sources of error based on their functional form. We then compute the sensitivity of the cosmological parameters to these functions through simulations. Finally, we compute the magnitude of each effect by summing the systematics for each category in quadrature. Table 8 summarizes the sensitivity of each parameter to each systematic. We also illustrate the effects of these systematic effects on the calculated parameters in graphical form.

### *Magnitude Offset Between Low- and High-z*

The low- and high-z observations are obtained on different telescopes, and therefore are calibrated independently, which can potentially introduce a simple magnitude offset between the zero-points of the low- and high-z data. We model this effect by simply adding fixed values, $\delta_m$, to the high-z peak magnitudes and re- compute the best-fit cosmology.

The results of this simulation are shown in Figure 20 and show that to a good approximation, the systematic effect of a magnitude offset on $w$ is a linear function of $\delta_m$ with slope $dw/d\delta_m = -2.69$ in the $i$-band and $dw/d\delta_m = -2.66$ in the $B$-band. Furthermore, there is no significant effect on the 3 nuisance parameters.

To estimate the value of $\delta_m$, we consider the following possible sources of such an offset: 1) error in the $Y$ and $J$ zero-points, 2) error in the $i$-band zero-point, and 3) errors in the extinction coefficients. We describe each in turn.

The contribution to the systematic uncertainty in $\delta_m$ has a different origin for the $Y$ and $J$ filters. As described in 4.4, we have used Kurucz models to extend the energy distributions of the Persson et al. (1998) standards from $J$ ($1.25\mu$) to $Y$ ($1.035\mu$) (Hamuy et al. 2006). That this was viable was confirmed by Contreras et al. (2009), who showed that the zero-color A0 star Feige 16 does in fact have $Y - J = -0.009 \pm 0.016$, confirming this calibration to an accuracy of $\pm 0.01$ mag. Conservatively, we adopt an error in the zero-point for the $Y$-band of $\pm 0.025$.

In the case of $J$, the main problem is the changing amount of water vapor above the telescope. An increase manifests itself as a systematic narrowing of the passband. This may or may not show up in standard star measurements, depending on when during the night they were measured. We adopt an error in the zero-point for $J$-band of $\pm 0.015$.

The common ancestor to the Persson et al. (1998) and Smith et al. (2002) systems is Vega. We therefore must determine the zero-point of the $i$-band relative to Vega instead of $BD + 17°4708$ in order to compute consistent zero-points. We have investigated the effects of a systematic error in the SED of Vega by comparing synthetic $i$-band photometry using the Bohlin (2007) and Bohlin & Gilliland (2004) SEDs. The difference is 0.01 mag. We further investigated uncertainties in our $i$-band filter transmission function. In constructing all our CSP filters, shifts in wavelength needed to be applied in order to have the synthetic color terms match the observed color terms (Contreras et al. 2009). A typical uncertainty in these shifts is approximately $10\mathring{A}$, which is equivalent to an error of $\pm 0.001$ mag. We therefore estimate a zero-point error of $\pm 0.01$ for the $i$-band.

According to Hamuy et al. (2006) and Contreras et al. (2009), the dispersion in the extinction coefficent for the $i$-band is $\pm 0.03$. The median airmass of our SNe Ia observations in the $i$-band was 1.315 and so we estimate a systematic error of $\pm 0.009$ mag due to dispersion in the extinction coefficient. Similar errors are expected for the $Y$- and $J$-band filters, though the median airmass for our high-redshift observations is typically lower (1.24). We therefore estimate a total error of $\pm 0.01$ mag.

Given the external check with the standard star Feige 16 (Contreras et al. 2009), we believe our calibration to be robust. Nevertheless, we allow for a conservative systematic magnitude offset between low- and high-redshift of $\delta_m = \pm 0.025$ mag.

### *Color Offset Between Low- and High-z*

This systematic is analogous to the magnitude offset and can occur for the same reasons; however, it propagates through the analysis differently as it is multiplied by the reddening coefficient. We proceed in the same manner as before, adding a color offset $\delta_c$ to the $(B - V)$ colors at high-z and compute the best-fit cosmology. As in the previous case, the effect on the cosmological parameters is linear (see Figure 21). However, the effect on the $B$-band is more than twice that in the $i$-band ($dw/d\delta_c = 2.53$ and $dw/d\delta_c = 7.53$, respectively). This is simply due to the fact that the reddening coefficient is twice as large at $B$ relative to the $i$-band. An advantage is that the colors we use in our analysis are all constructed from the same optical photometric systems and avoid the NIR and $i$-band. We estimate the total possible color offset to be $\delta_c = \pm 0.02$.

### *Color Gradient*

Color terms are used to transform the magnitudes of the standard stars to the natural CSP system. These color terms are empirically determined and therefore suffer from measurement uncertainty. An error in the color terms could potentially introduce a color gradient in the data: color errors that correlate with the instrumental color of the SNe Ia. Figure 23 shows the sensitivity functions. As expected, the impact in the $B$-band is larger than in the $i$-band. From Hamuy et al. (2006) and Contreras et al. (2009), we estimate $\delta\,(CT) = 0.015$, which is the typical 1-$\sigma$ error in the color terms.

*Estimation of Uncertainties*

The method of $\chi^2$-minimization suffers from a well-known bias when there is measurement error in the independent variables (Kelly 2007). The root of the problem lies in the fact that the numerator of $\chi^2$ (see equation 4) is sensitive to the model parameters only, whereas the denominator is sensitive to the nuisance parameters as well as the variances (see equation 5). As such, the best-fit solution is a function not only of the data, but the variances as well, complicating the computation of the overall systematic uncertainties.

We have investigated the effect of adding extra variance to both the colors $\sigma_c^2$ and $\Delta m_{15}$. Figure 22 shows the strong dependence of $R_V$ on $\sigma_c$. The $i$-band data are about a factor of two less sensitive to changes in $R_V$ than the $B$-band data. As a result, the bias due to the denominator of $\chi^2$ is larger in the $i$-band. If we were to include more heavily reddened objects (for instance SN 2005A and SN 2006X), then this effect would disappear entirely. The effects of extra variance in $\Delta m_{15}$ are not significant and are therefore not shown, though they are included in Table 8 for completeness.

REFERENCES


Albrecht, A., et al. 2006, astro-ph/0609591, (DETF Report)
Astier, P., et al. 2006, A&A, 447, 31
Balland, C., et al. 2006, A&A, 445, 387
Bertin, E., & Arnouts, S. 1996, A&AS, 117, 393
Blandford, R. D. 2004, Measuring and Modeling the Universe, Cambridge University Press, as part of the Carnegie Observatories Astrophysics Series, edited by W. L. Freedman, p. 377
Blondin, S., et al. 2006, AJ, 131, 1648
Bohlin, R. C., & Gilliland, R. L. 2004, AJ, 127, 3508
Bohlin, R. C., Bohlin, R. C. 2007, in The Future of Photometric, Spectrophotometric, and Polarimetric Standardization, ASP Conf. Series, Vol. 364, p. 315, ed. C. Sterken.
Burns, C. R., et al. 2009, in preparation.
Cardelli, J. A., Clayton, G. C., & Mathis, J. S. 1989, ApJ, 345, 245
Caldwell, R. R., & Kamionkowski, M. 2004, Journal of Cosmology and Astro-Particle Physics, 9, 9
Conley, A., et al. 2008, ApJ, 681, 482
Contreras, C., et al. 2009, AJ, submitted.
Draine, B. T. 2003, ARA&A, 41, 241
Eisenstein, D. J., et al. 2005, ApJ, 633, 560
Elias, J. H., Frogel, J. A., Matthews, K., & Neugebauer, G. 1982, AJ, 87, 1029
Elias, J. H., Matthews, K., Neugebauer, G., & Persson, S. E. 1985, ApJ, 296, 379
Ellis, R. S. et al., 2008, ApJ, 674, 51
Folatelli, G., et al. 2006, ApJ, 641, 1039
Folatelli, G., et al. 2009, AJ, submitted.
Foley, R. J., et al. 2008, ApJ, 684, 68
Frieman, J. A., Turner, M. S., & Huterer, D., 2008, ARA&A, 46, 385
Frieman, J. A., et al. 2008, AJ, 135, 338
Freedman, W. L., et al. 2001, ApJ, 553, 47
Gallagher, J. S., et al. 2008, arXiv:0805.4360
Goobar, A., 2008, arXiv:0809.1094
Hamuy, M., Phillips, M. M., Maza, J., Suntzeff, N. B., Schommer, R. A., & Aviles, R. 1995, AJ, 109, 1
Hamuy, M., Phillips, M. M., Suntzeff, N. B., Schommer, R. A., Maza, J., & Aviles, R. 1996a, AJ, 112, 2398
Hamuy, M., Phillips, M. M., Suntzeff, N. B., Schommer, R. A., Maza, J., Smith, R. C., Lira, P., & Aviles, R. 1996b, AJ, 112, 2438
Hamuy, M., Phillips, M. M., Suntzeff, N. B., Schommer, R. A., Maza, J., & Aviles, R. 1996c, AJ, 112, 2391
Hamuy, M., Trager, S. C., Pinto, P. A., Phillips, M. M., Schommer, R. A., Ivanov, V., & Suntzeff, N. B. 2000, AJ, 120, 1479
Hamuy, M., et al. 2006, PASP, 118, 2
Hawkins, E. et al. 2003, MNRAS, 346, 78
Hillenbrand, L. A., Foster, J. B., Persson, S. E., & Matthews, K. 2002, PASP, 114, 708
Holtzman, J. A., et al. 2008, AJ, 136, 2306
Holz, D. E. 1998, ApJ, 506, L1
Hook, I. M., et al. 2005, AJ, 130, 2788
Hsiao, E. Y., Conley, A., Howell, D. A., Sullivan, M., Pritchet, C. J., Carlberg, R. G., Nugent, P. E., & Phillips, M. M. 2007, ApJ, 663, 1187
Kasen, D. 2006, ApJ, 649, 939
Jha, S., Riess, A. G., & Kirshner, R. P. 2007, ApJ, 659, 122
Kelly, B. C. 2007, ApJ, 665, 1489
Kelson, D., Burns, C. R., & Walth, G. 2009, in preparation
Kim, A., Goobar, A., & Perlmutter, S. 1996 PASP, 108, 190
Knop, R. A., et al. 2003, ApJ, 598, 102
Krisciunas, K., et al. 2001, AJ, 122, 1616
Krauss, L. M., & Chaboyer, B. 2003, Science, 299, 65
Landolt, A. U. 1992, AJ, 104, 340
Linder, E. V. 2006, Astroparticle Physics, 26, 102
Lira, P. 2005, Master's Thesis, University of Chile
Madore, B. F. 1982, ApJ, 253, 575
Martini, P., Persson, S. E., Murphy, D. C., Birk, C., Shectman, S. A., Gunnels, S. M., & Koch, E. 2004, Proc. SPIE, 5492, 1653
Matheson, T., et al. 2005, AJ, 129, 2352
Meikle, W. P. S. 2000, MNRAS, 314, 782
Miknaitis, G., et al. 2007, ApJ, 666, 674
Naylor, T., 1996, MNRAS, 296, 339
Nobili, S., et al. 2005, A&A, 437, 789
Nobili, S., & Goobar, A., 2008, A&A, 487, 19
Nugent, P., Kim, A., & Perlmutter, S. 2002, PASP, 114, 803
Perlmutter, S., et al. 1999, ApJ, 517, 565
Persson, S. E., Murphy, D. C., Krzeminski, W., Roth, M., & Rieke, M. J. 1998, AJ, 116, 2475
Phillips, M. M. 1993, ApJ, 413, L105
Phillips, M. M., Lira, P., Suntzeff, N. B., Schommer, R. A., Hamuy, M., & Maza, J. 1999, AJ, 118, 1766
Phillips, M. M., et al. 2007, PASP, 119, 360
Pinto, P. A., & Eastman, R. G. 2000, ApJ, 530, 757
Prieto, J. L., Rest, A., & Suntzeff, N. B. 2006, ApJ, 647, 501
Riess, A. G., Press, W. H., & Kirshner, R. P. 1996, ApJ, 473, 88
Riess, A. G., et al. 1998, AJ, 116, 1009
Riess, A. G., et al. 2000, ApJ, 536, 62
Riess, A. G., et al. 2004, ApJ, 607, 665
Riess, A. G., et al. 2007, ApJ, 659, 98
Sako, M., et al. 2008, AJ, 135, 348
Schlegel, D. J., Finkbeiner, D. P., & Davis, M. 1998, ApJ, 500, 525
Smith, J. A., et al. 2002, AJ, 123, 2121
Spergel, D. N., et al. 2003, ApJS, 148, 175
Spergel, D. N., et al. 2007, ApJS, 170, 377
Stetson, P. B., 1990, PASP, 102, 932
Sullivan, M., et al. 2003, MNRAS, 340, 1057
Tremaine, S. et al. 2002, ApJ, 574, 740
Tripp, R. 1998, A&A, 331, 815
Tripp, R., & Branch, D. 1999, ApJ, 525, 209
Wood-Vasey, W. M., et al. 2007, ApJ, 666, 694
Wang, L., Strovink, M., Conley, A., Goldhaber, G., Kowalski, M., Perlmutter, S., & Siegrist, J. 2006, ApJ, 641, 50
York, D. G., et al. 2000, AJ, 120, 1579

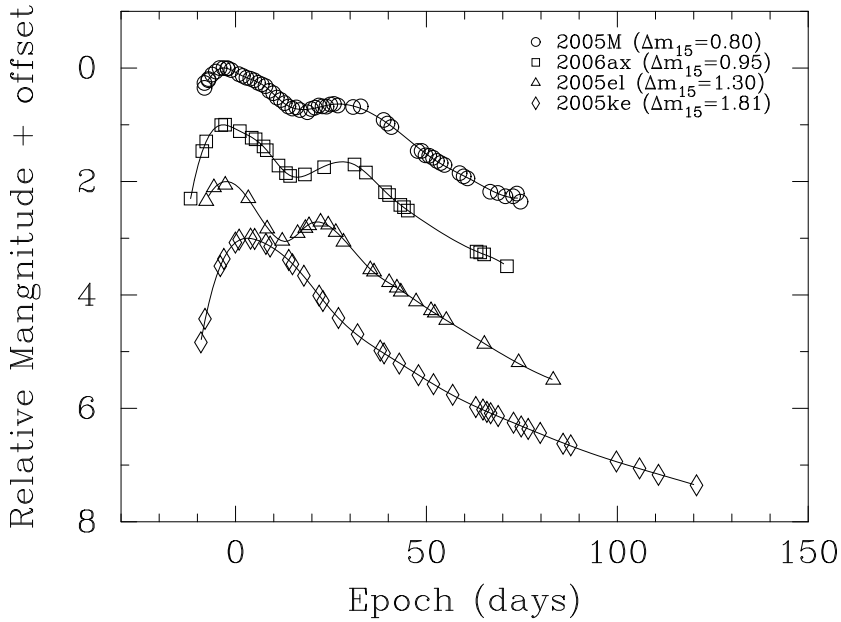


FIG. 1.— A representative sample of four $i$-band lightcurves from the low-z CSP sample chosen to illustrate the behavior of the secondary maximum. For clarity, the lightcurves have been normalized to their peak magnitudes and then offset by one magnitude from each another. The SNe Ia have values of $\Delta m_{15}$ ranging from 1.12 to 1.81. The fast-declining SN Ia with $\Delta m_{15} = 1.81$ (bottom light curve) shows no secondary maximum.

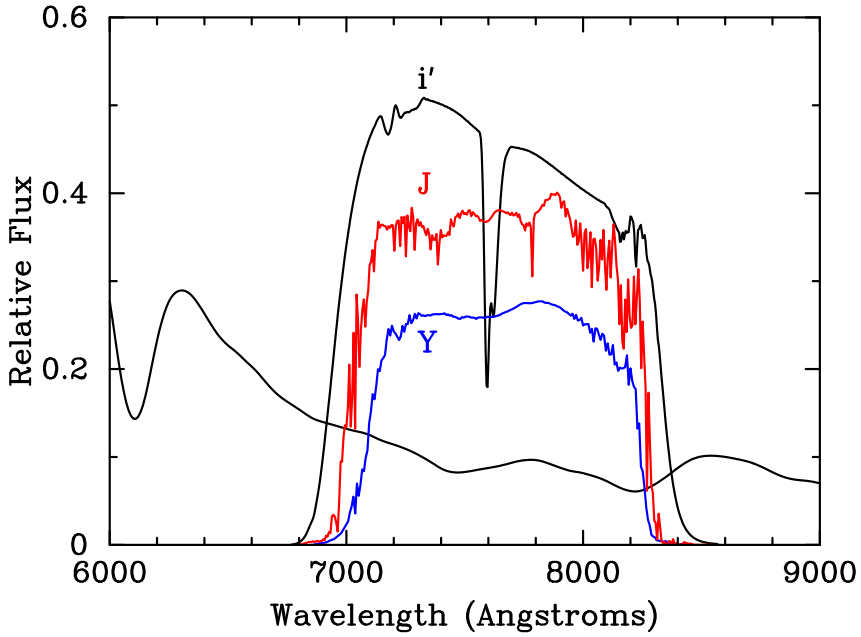


FIG. 2.— Filter response functions for the $Y$ (blue) and $J$ (red) bands blueshifted by 0.35 and 0.63, respectively. Rest-frame $i$-band is plotted in black. The absorption feature at $\lambda \sim 7600\AA$ is telluric $O_2$. Crossing the entire figure, the SED of a typical SN Ia at maximum (Hsiao et al. 2007) is also shown in black.

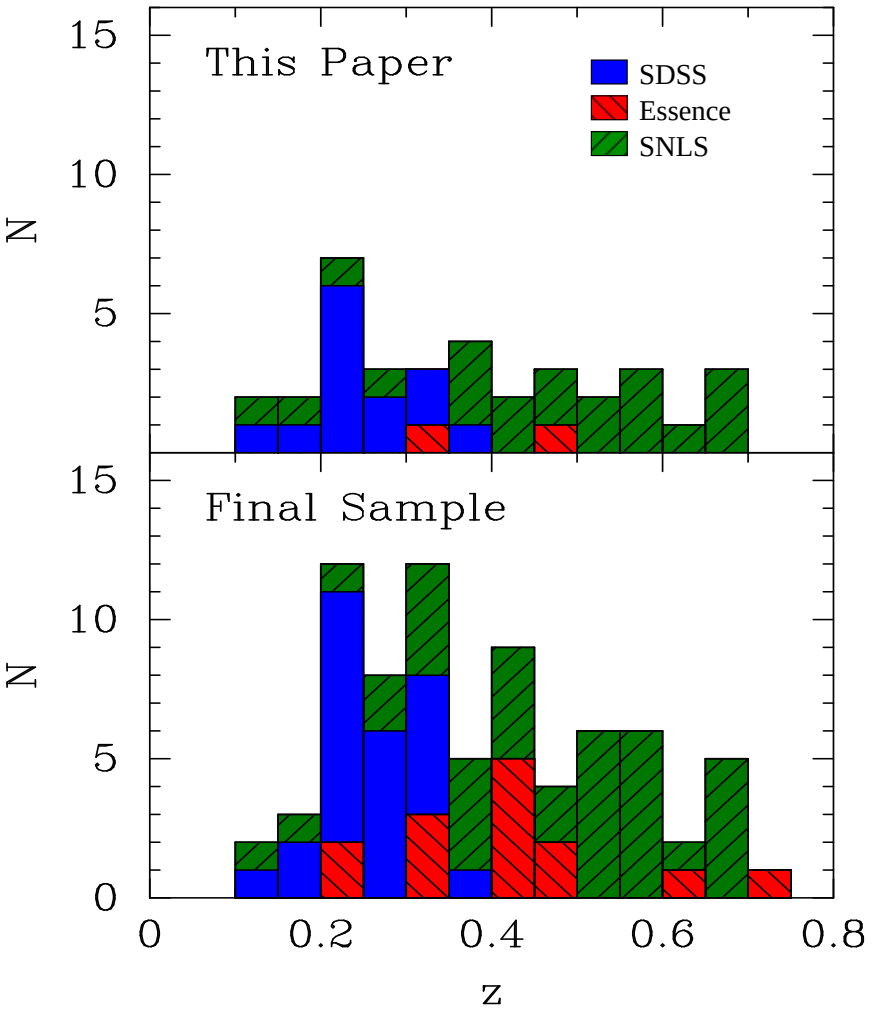


Fig. 3.— Redshift distribution of objects observed as part of the CSP in the NIR on Magellan. In general, the higher-redshift objects are found by the SNLS, and those at lower redshifts primarily by the SDSS-II. We have observed 14 objects discovered by ESSENCE, 37 SNLS objects and 24 SDSS objects.

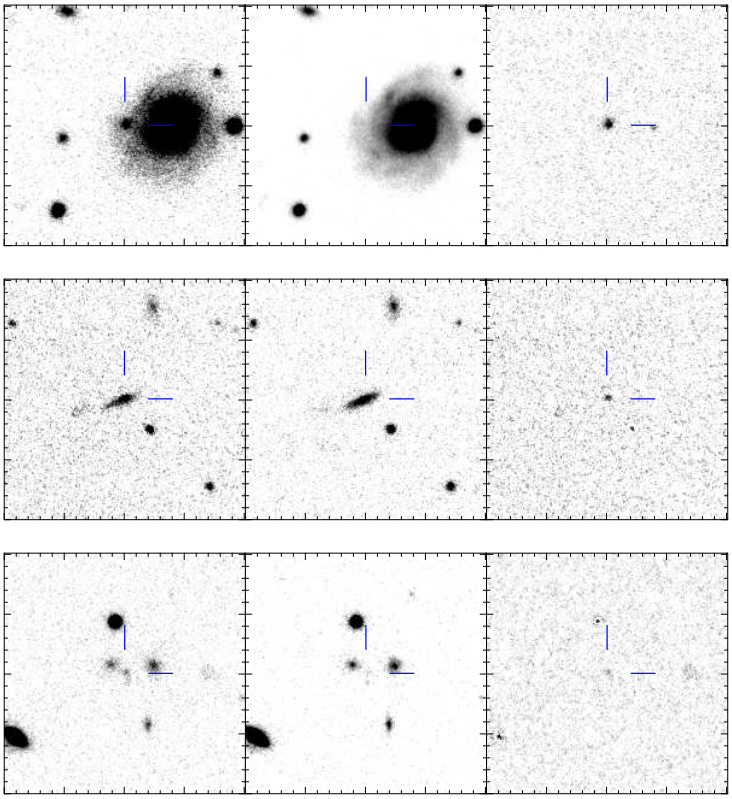

FIG. 4.— Sample of SNe Ia, post-SNe Ia and difference frames for three SNe Ia: SN 3241 (discovered by SDSS-II, top panel), 04D1rh (discovered by SNLS, middle panel), and 05D2bt (discovered by SNLS, bottom panel). SN 3241 ($z = 0.25$) was observed in the Y-band, 04D1rh ($z = 0.435$) was observed in both Y and J (J is shown), and 05D2bt ($z = 0.679$) was observed in the J-band. The scale of these images is 200 pixels = 25 arc-seconds on a side.

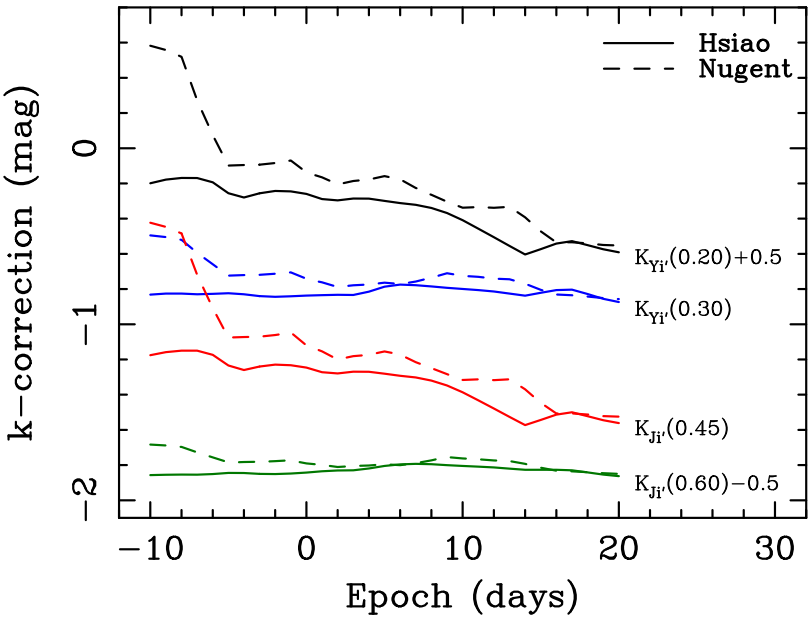


FIG. 5.— Cross-band K-corrections ($K_{iJ}$ and $K_{iY}$), based on SED templates of Hsiao et al. (2007) and Nugent et al. (2002), shown as a function of epoch for redshifts z = 0.20, 0.30, 0.45 and 0.60. The solid lines are the Hsiao et al. corrections and the dashed lines are Nugent et al. The largest differences occur at about 10 days before maximum. Given the significantly larger template library available to Hsiao et al., and the corrections for the telluric features, we have adopted the Hsiao et al. corrections.

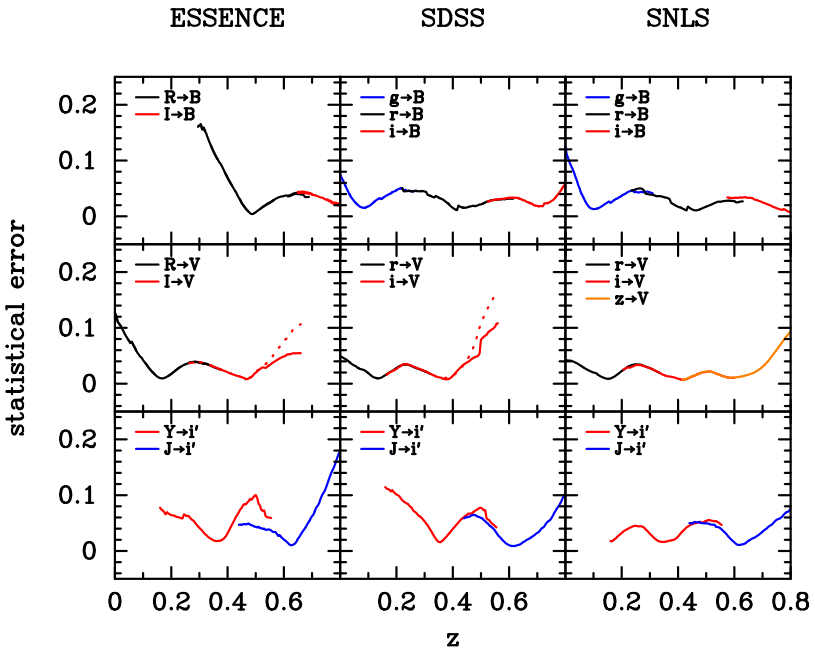


FIG. 6.— Estimated dispersion in the K-corrections as a function of redshift for different photometric filter sets. Solid lines represent the dispersion when full optical and NIR filter sets are used to color-correct the template SED, whereas dashed lines show the dispersions when no NIR data are included. The dispersion in the $K_{RB}$ for ESSENCE increases dramatically at low redshift because $R_{4m}$ is redder than rest-frame $B$ and there are therefore no observations to anchor the SED template on the blue side to which we are transforming. Our lowest redshift ESSENCE object in this analysis is at z = 0.34. At the high-redshift end, the uncertainty for $K_{IV}$ is higher since $I_{4m}$ is shifted to the blue side of rest $i$, and there is no anchor on the red side. Adding the NIR photometry helps in the color-matching and decreases the dispersion. There is little effect on the SNLS dispersions because our CSP sample includes only objects with redshifts less than 0.8 and the $z_m$ band serves as a red anchor over this entire range.

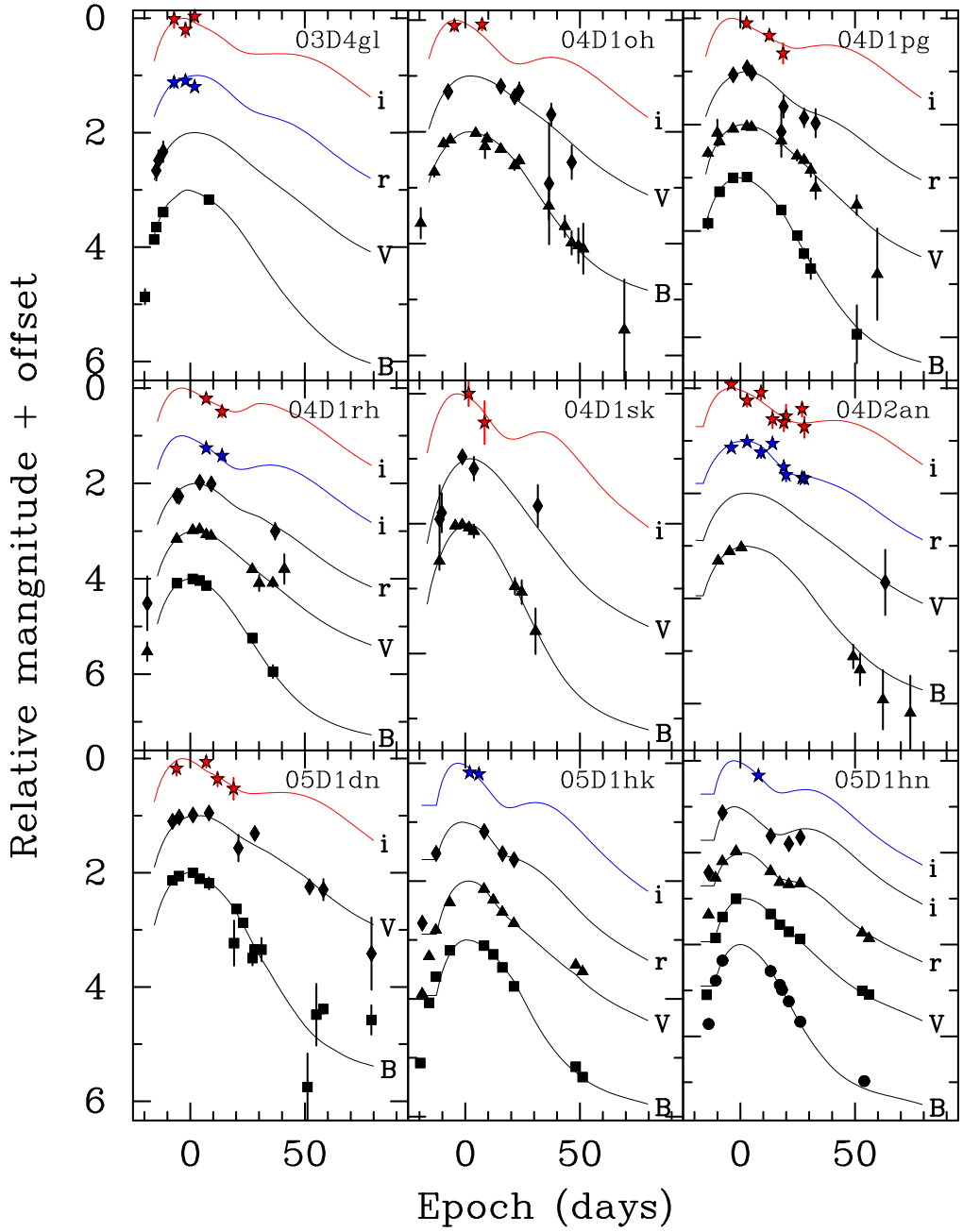


FIG. 7.— Optical and $YJ$-band light curves for SNe Ia discovered as part of the SNLS, ESSENCE and SDSS-II projects, followed up using PANIC on Magellan. Light curves and templates are shown in the observer (not rest) frame. The template $BVri$ light curves (solid lines) are based on the low-redshift CSP data (Folatelli et al. 2009), and are expanded by $(1+z)$ and K-corrected to fit the observed light curves. The curves are labelled $BVri$ to indicate which restframe template has been used to fit the observed data. An offset of 1 mag is applied so that the curves do not intersect. In some cases, both the observed $Y$ and $J$ data are de-redshifted to the $i$ band. The maximum-light magnitudes for each filter are presented in Table 5. The red and blue stars correspond to the CSP's J- and Y-band data, respectively. The black circles correspond to $g_m$ (SNLS) or $g_s$ (SDSSII); the black squares correspond to $r_m$ (SNLS), $r_s$ (SDSSII), or $R_{4m}$ (ESSENCE); the black triangles correspond to $i_m$ (SNLS), $i_s$ (SDSSII), or $I_{4m}$ (ESSENCE); and the black diamonds correspond to $z_m$ (SNLS).

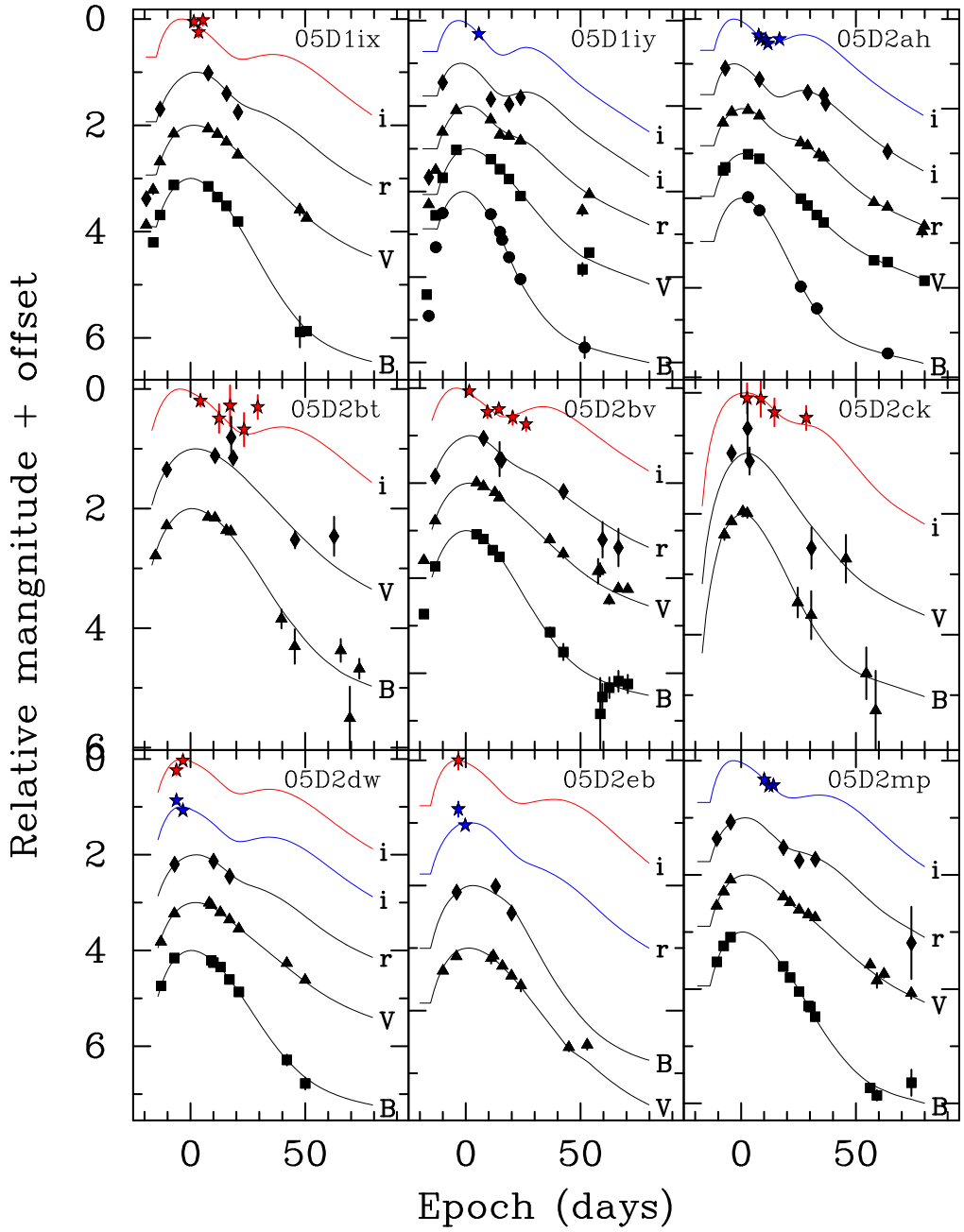


Fig. 8.— Same as Figure 7.

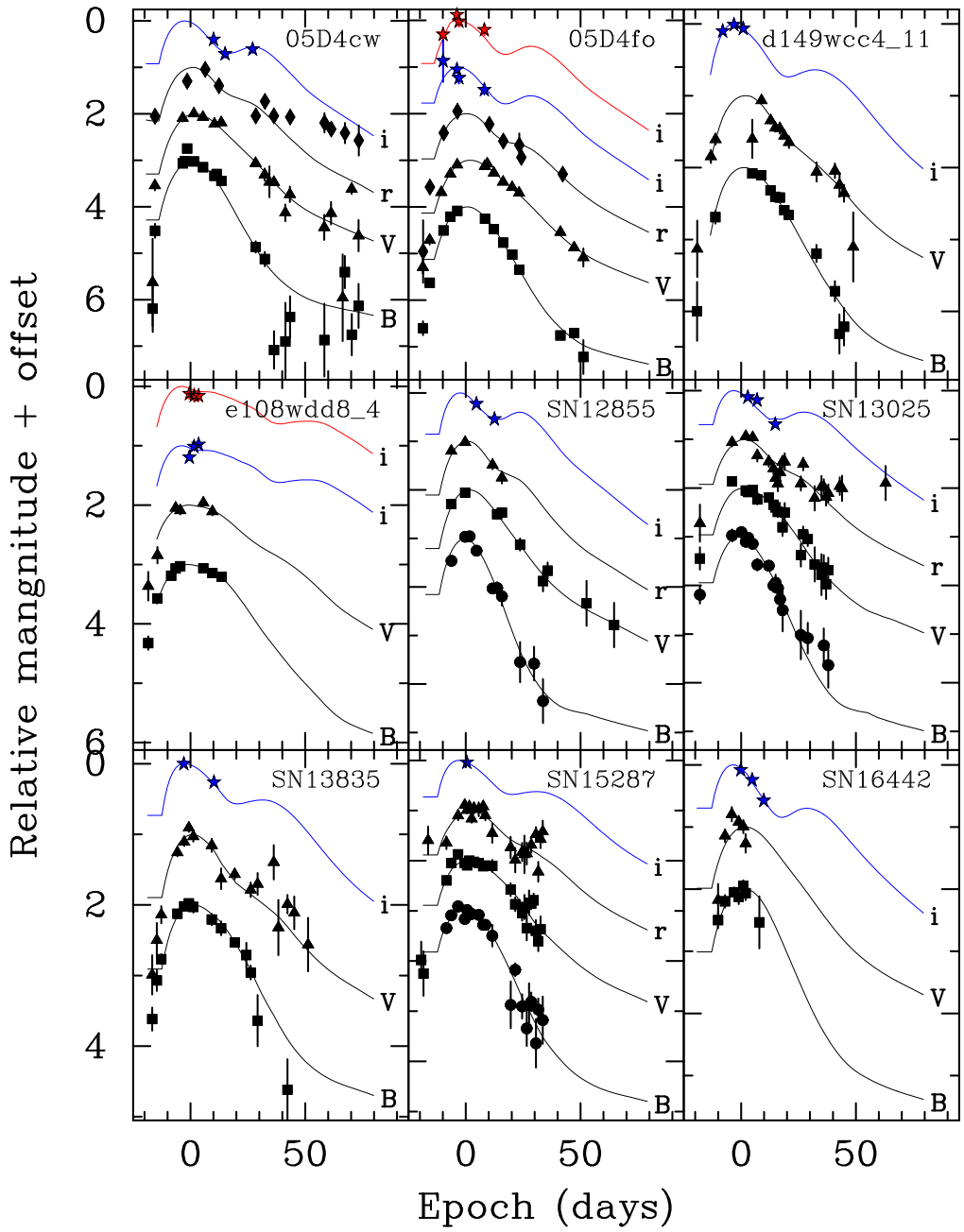


Fig. 9.— Same as Figure 7.

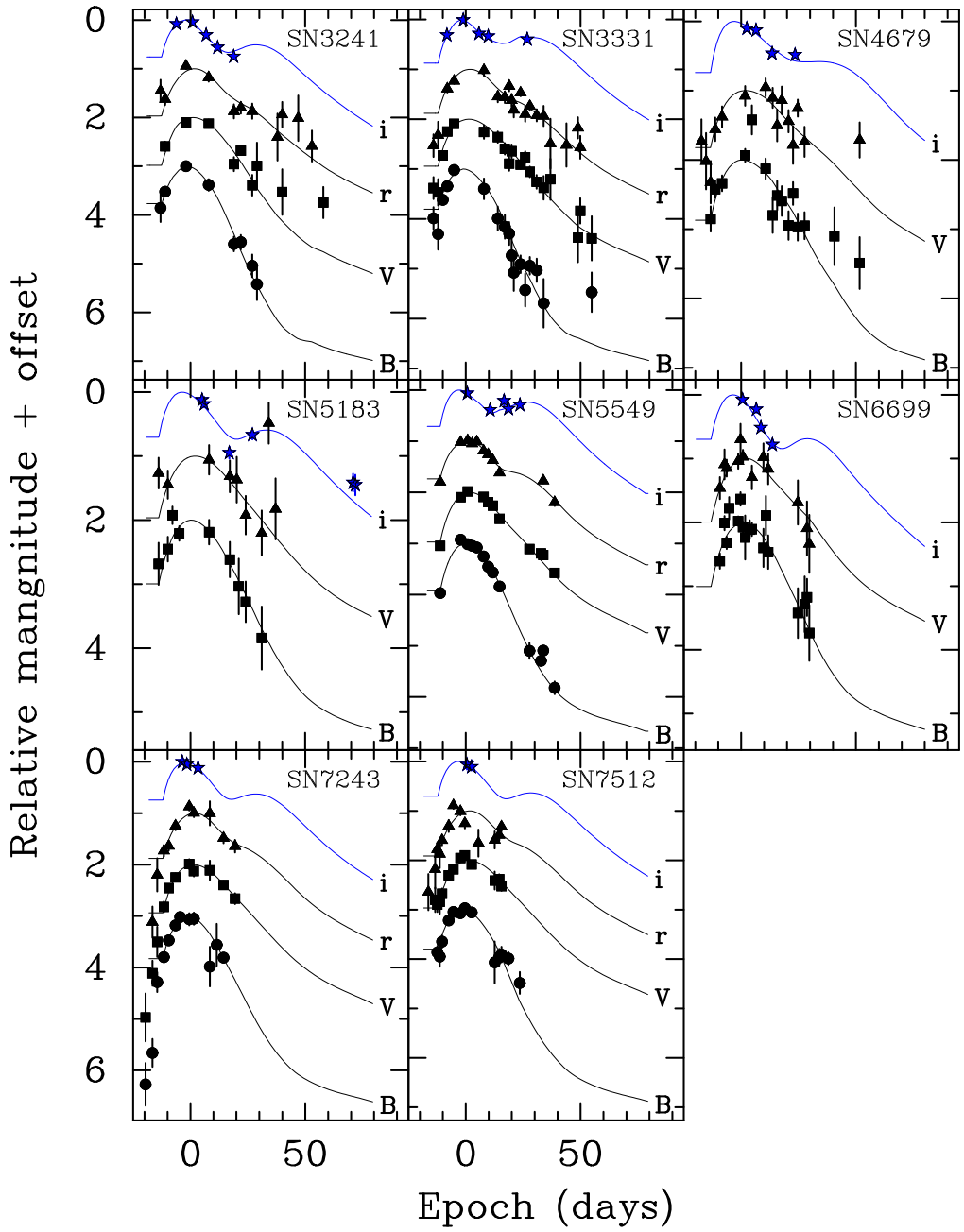


Fig. 10.— Same as Figure 7.

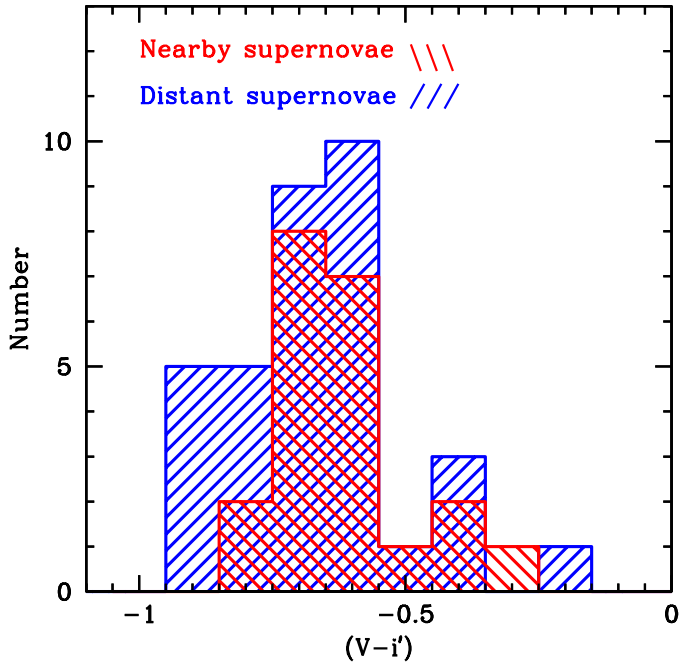


FIG. 11.— Histograms of the $(V-i)$ color distributions at low and high redshifts for the SNe Ia labeled best observed in Table 1 of Folatelli et al. (2009)), with redshifts z > 0.01, and with $E(B-V) < 0.5$ mag. Note that the $(V-i)$ colors on our natural system are all negative, and bluer than $(V-I)$. The object SN 04D2an is not included in this plot as it has no rest-frame $V$ observation.

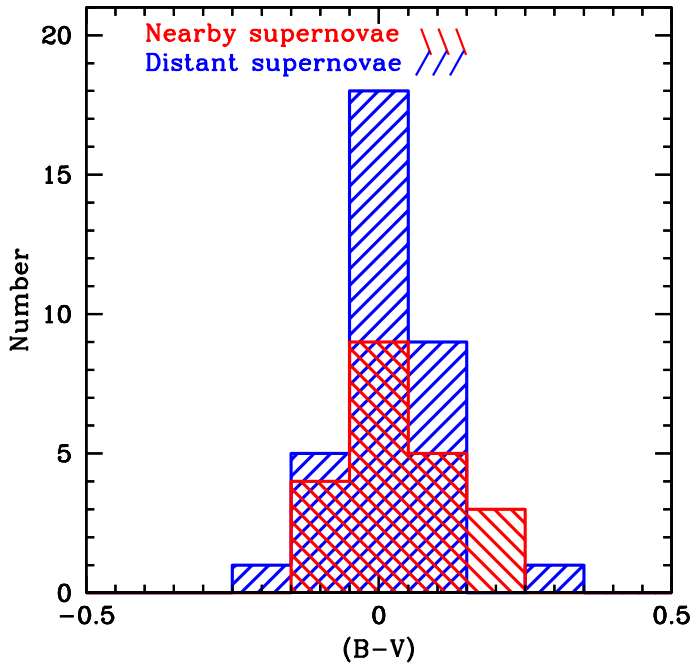


FIG. 12.— Histograms of the $(B-V)$ color distributions at low and high redshifts.

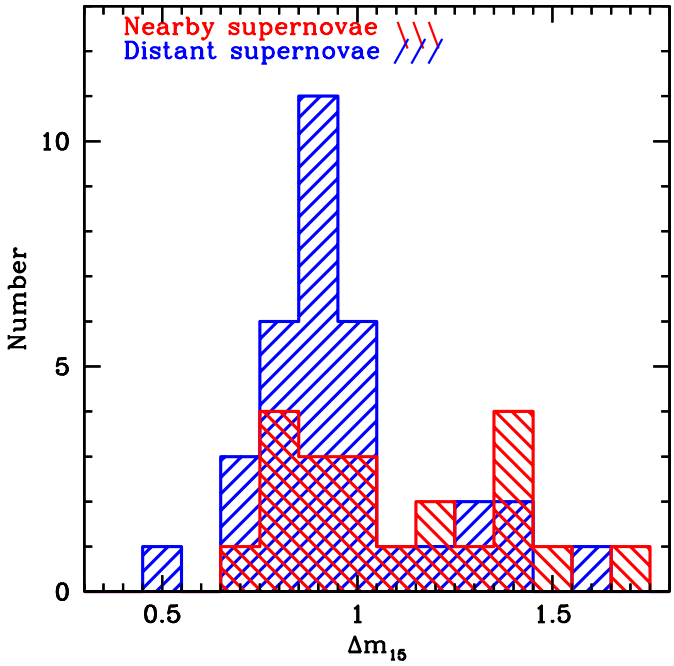


FIG. 13.— Histograms of the $\Delta m_{15}$ distributions at low and high redshifts.

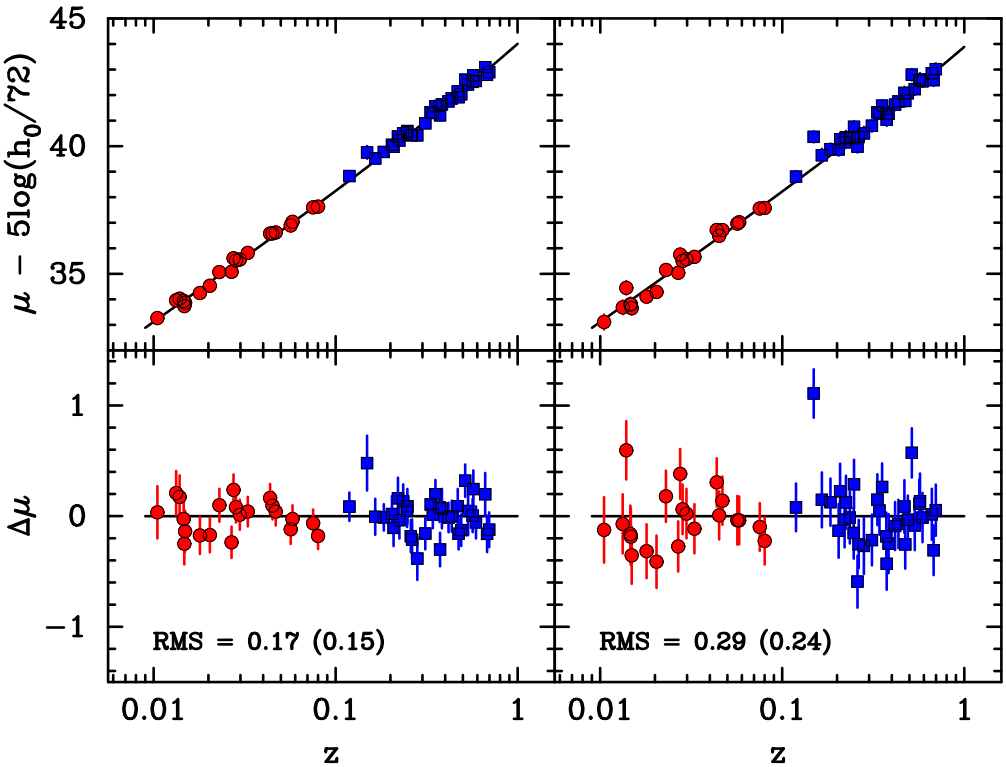


FIG. 14.— Top panel: $i$ and $B$-band Hubble diagrams for 21 low-redshift and 35 high-redshift SNe Ia from the CSP, *uncorrected for reddening*. Bottom panel: The residuals about the best-fit to these data. The values for *rms* scatter about the best fit to these data are labelled. The *rms* value in brackets excludes the most discrepant (highly reddened) SNLS 05D1hn.

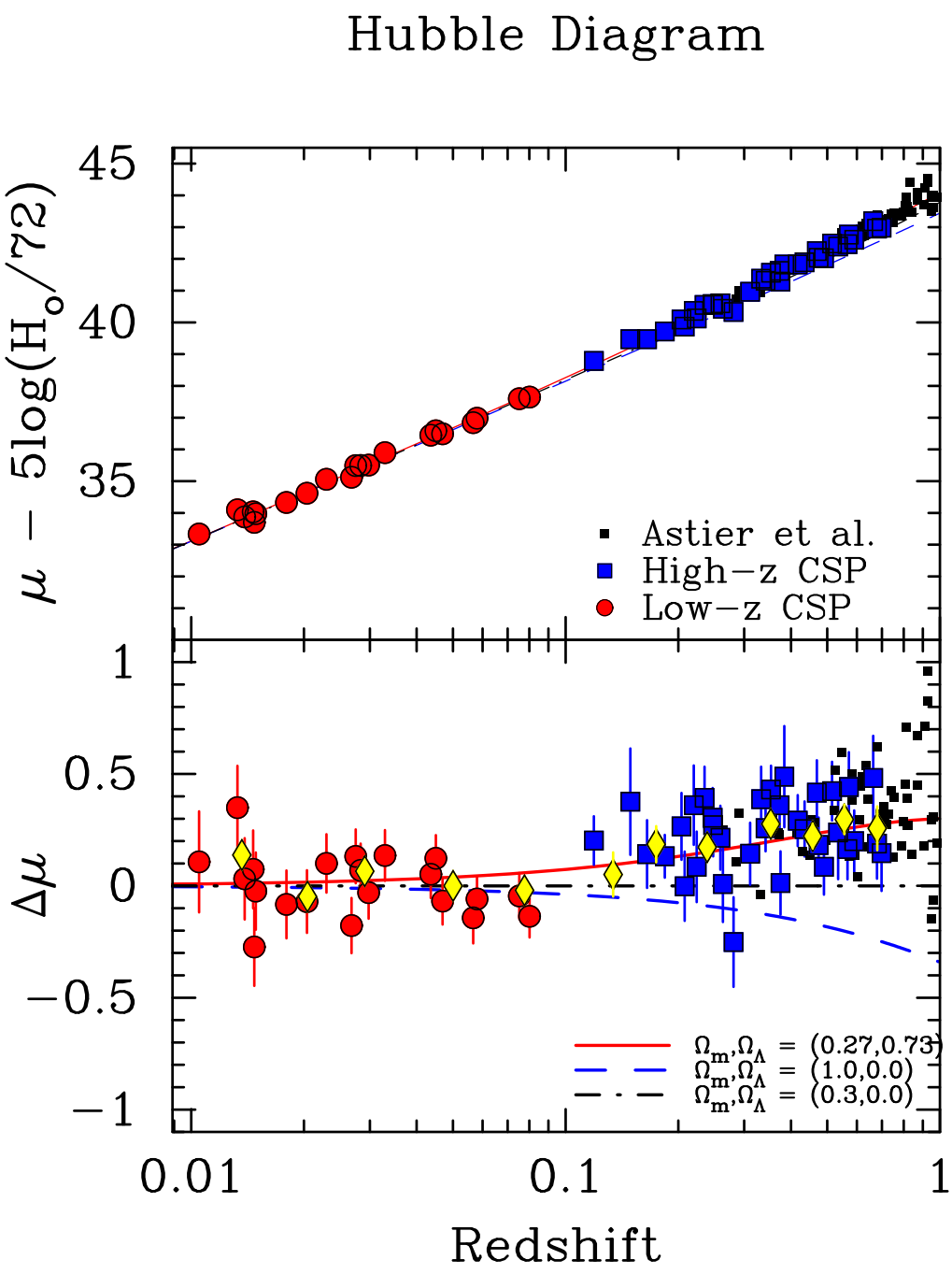


FIG. 15.— $i$-band rest-frame Hubble diagram for a total of 56 CSP SNe Ia, 35 SNe Ia from the Magellan CSP sample (blue squares), and 21 low-redshift data (red solid circles) from Folatelli et al. (2009). For comparison, distances determined by Astier et al. (2006) are shown as black squares, but are not included in the fits. Error bars shown are 1-$\sigma$. A value of $H_0 = 72$ km s$^{-1}$ Mpc$^{-1}$ has been adopted for the plot. The solid (red), dot-dashed (black), and dashed (blue) lines represent $\Omega_m = 0.3$, $\Omega_{DE} = 0.7$ ; $\Omega_m = 0.3$, $\Omega_{DE} = 0$ ; and $\Omega_m = 1$ models, respectively. The data are consistent with the standard (accelerating) cosmological model. To minimize the effects of peculiar velocities, the fit to the low-redshift sample is restricted to z>0.010. In the bottom panel, the data are shown relative to the standard model, shown as the solid line. The yellow diamonds are the result of binning the data (see table 6).

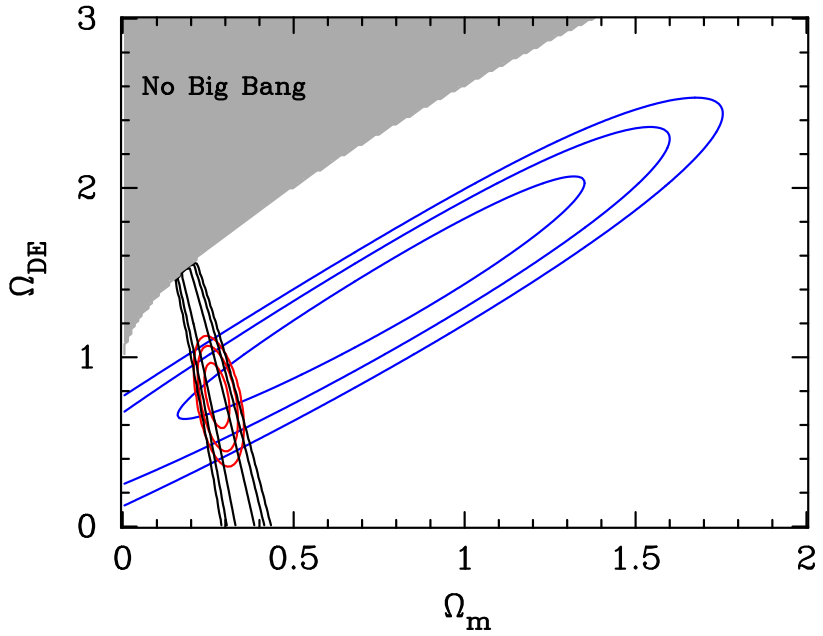


FIG. 16.— Our best-fit cosmological model in the $\Omega_m$–$\Omega_{DE}$ plane assuming a constant equation of state parameter $w = -1$. Our 68%, 95%, and 99% confidence intervals are shown as solid blue (diagonal) contours. The constraints from baryon acoustic oscillations (Eisenstein et al. 2005) are shown as solid black (nearly-vertical) contours and the combined confidence intervals are shown as red contours.

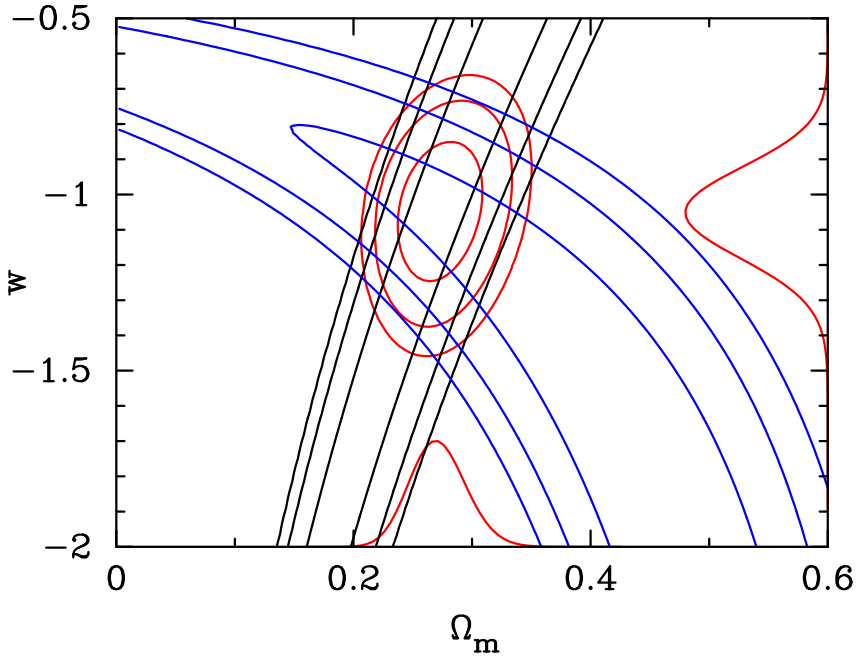


FIG. 17.— Combining the CSP constraints with baryonic acoustic oscillations (Eisenstein et al. 2005) and assuming $\Omega_k = 0$. The CSP and BAO data combined are consistent with a value of $w = -1.05 \pm 0.13$ (statistical) $\pm 0.09$ (systematic) and $\Omega_m = 0.27 \pm 0.02$ (statistical). Our 68%, 95%, and 99% confidence intervals are shown as solid blue (banana-shaped) contours. The constraints from baryon acoustic oscillations (Eisenstein et al. 2005) are shown as solid black contours and the combined confidence intervals are shown as red contours. The 1-D marginalized probabilities for each parameter are plotted as red lines on the axes.

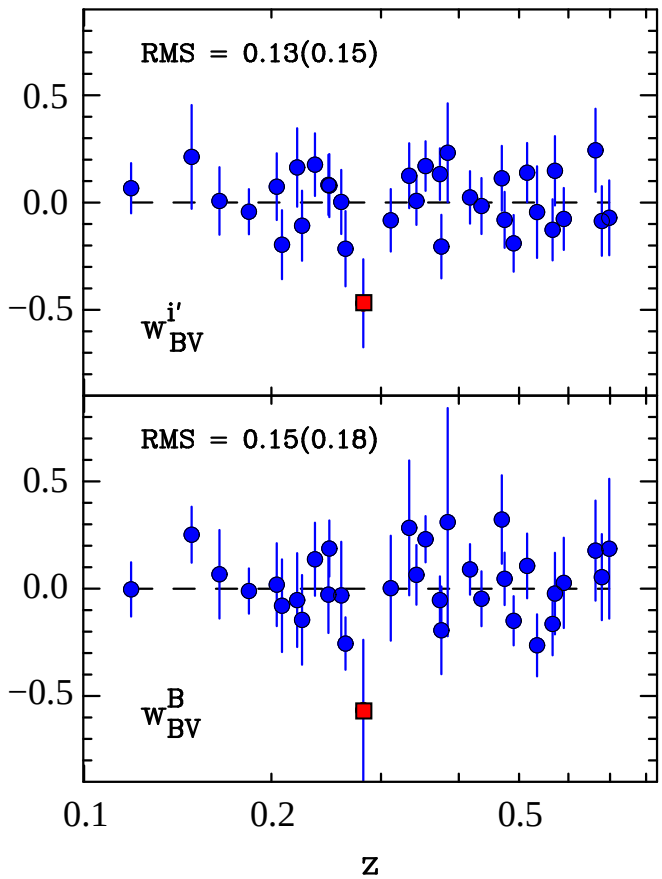


FIG. 18.— Residuals in the $i$ and $B$ Hubble diagrams. The top panel shows reddening-free $i$ magnitudes and the bottom panel shows the reddening-free $B$ magnitudes. Both are computed using the $(B-V)$ color. The *rms* dispersion is shown in the upper left. SN 04D2an is not shown as it has no $V$-band observation. If one includes SN 16442 (red square), the dispersion in the Hubble diagram increases to $\pm 0.15$ at $i$, and $\pm 0.18$ at $B$ as indicated in parentheses. The dashed line correponds to the best-fit cosmological model.

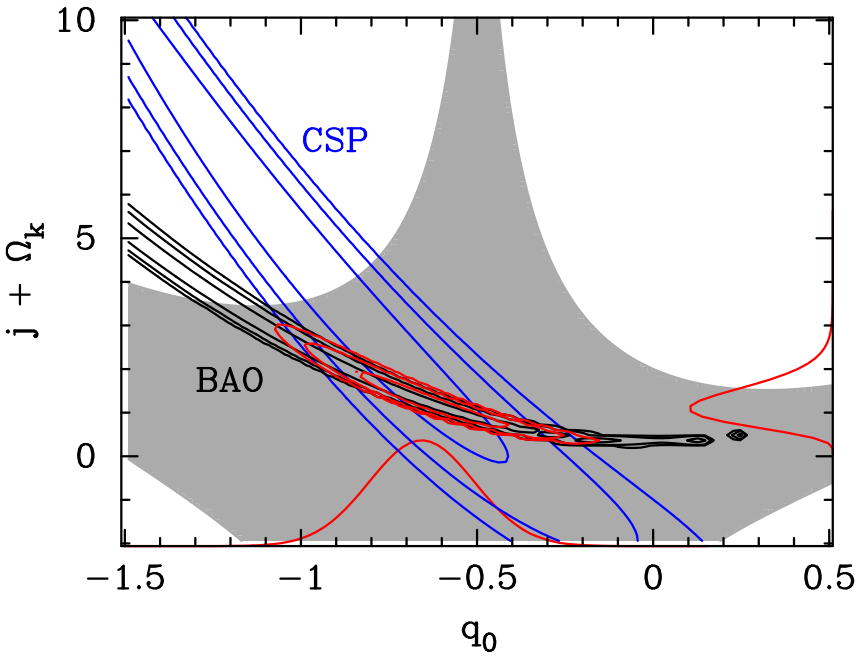


FIG. 19.— The sum ($j_k$) of the jerk ($j$) and curvature parameter ($\Omega_k$) as a function of the deceleration parameter ($q_0$). The grey shading indicates the region where the luminosity distance expansion is valid, as described in the text. The best-fit values including both baryon acoustic oscillation and the CSP data are $j_k = 1.18 \pm 0.44$ (statistical) $\pm\, 0.27$ (systematic) and $q_o = -0.67 \pm 0.13$ (statistical) $\pm$ 0.09 (systematic) at the 95% confidence level. The 1-D marginalized probabilities for each parameter are plotted as red lines on the axes.

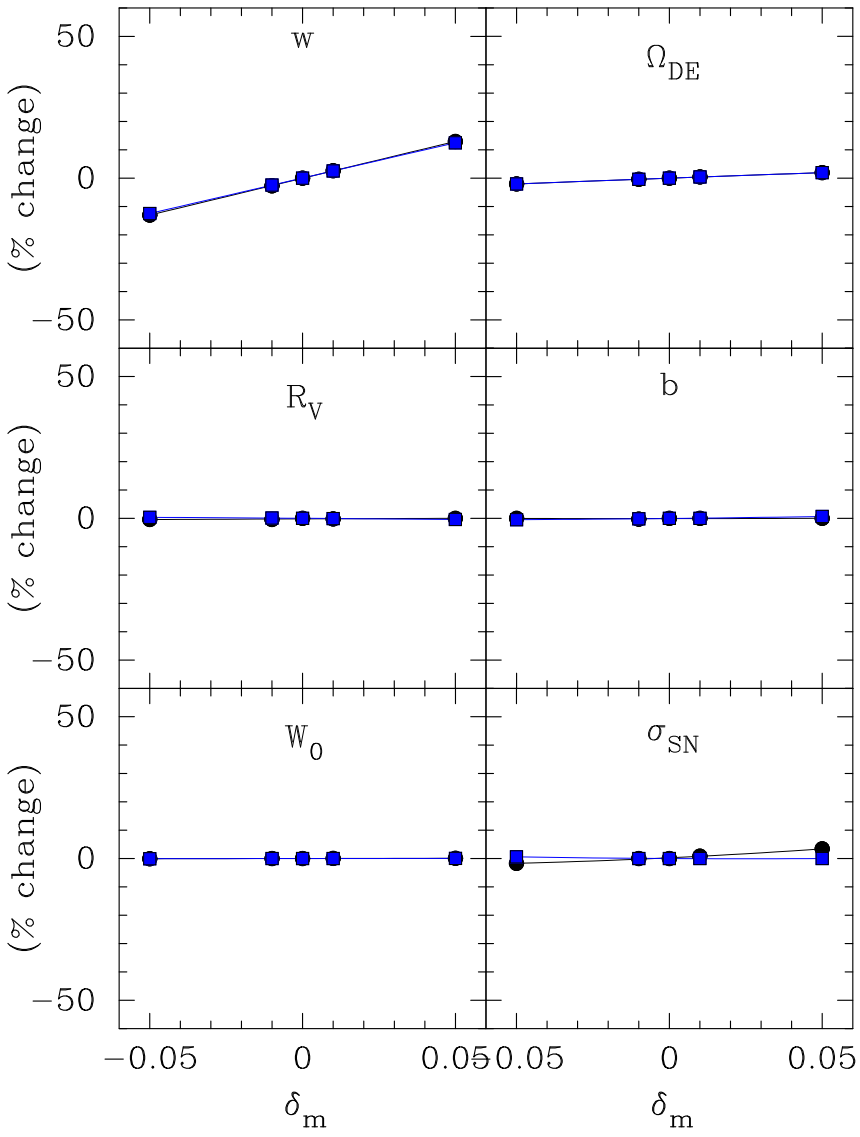


FIG. 20.— The effect of a magnitude offset $\delta_m$ on the best-fit parameters, $w$, $\Omega_{DE}$, $R_V$, $B$, $W_0$, and $\sigma_{SN}$. The black circles are for i-band, while the red squares are for $B$-band. In almost all cases, the differences in the points are negligible. The lines are quadratic fits. The largest sensitivity to a magnitude offset is for $w$. For an offset of 0.025 magnitudes, the percentage change in $w$ amounts to 7%.

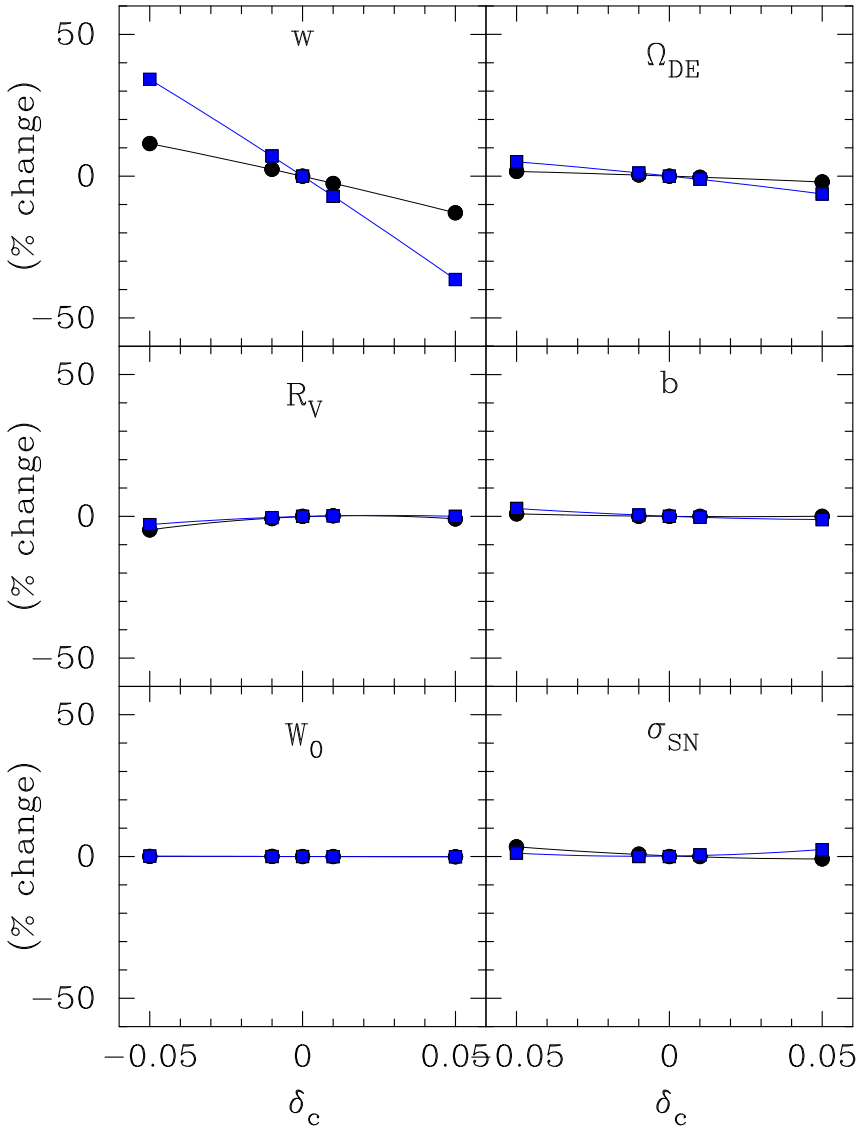


FIG. 21.— The effect of a color offset $\delta_c$ on the best-fit parameters, as listed in Figure 20. The black circles are for i-band, while the red squares are for $B$-band. The lines are quadratic fits. The largest sensitivity to a color offset is again for $w$. For a color offset of 0.02 magnitudes, the percentage change in $w$ amounts to 5%.

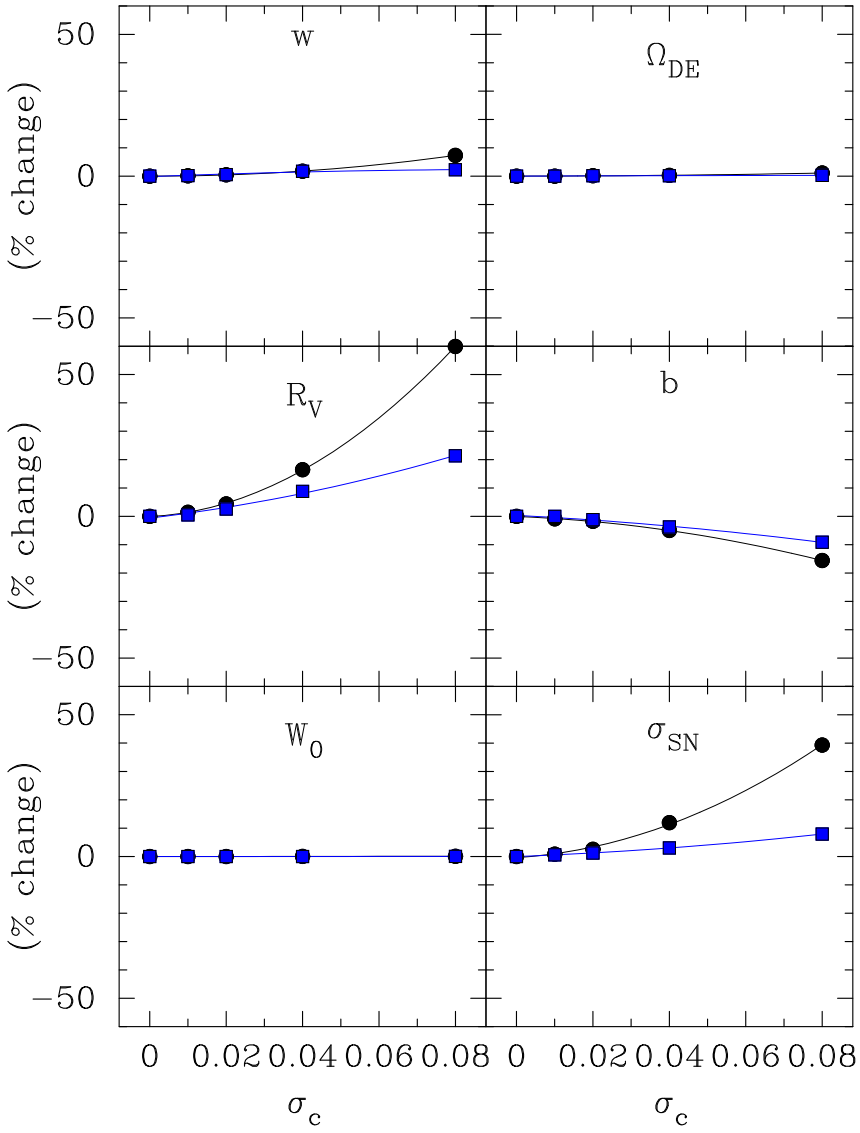


FIG. 22.— The effect of extra variance in the color measurements $\sigma_c$ on the best-fit parameters, as listed in Figure 20. The black circles are for i-band, while the red squares are for $B$-band. The lines are quadratic fits. A variance in the color measurements impacts the determination of the reddening law or color term. A variance of $\pm 0.03$ magnitudes results in a percentage change in $R_V$ of 10%. The impact on cosmology is very small.

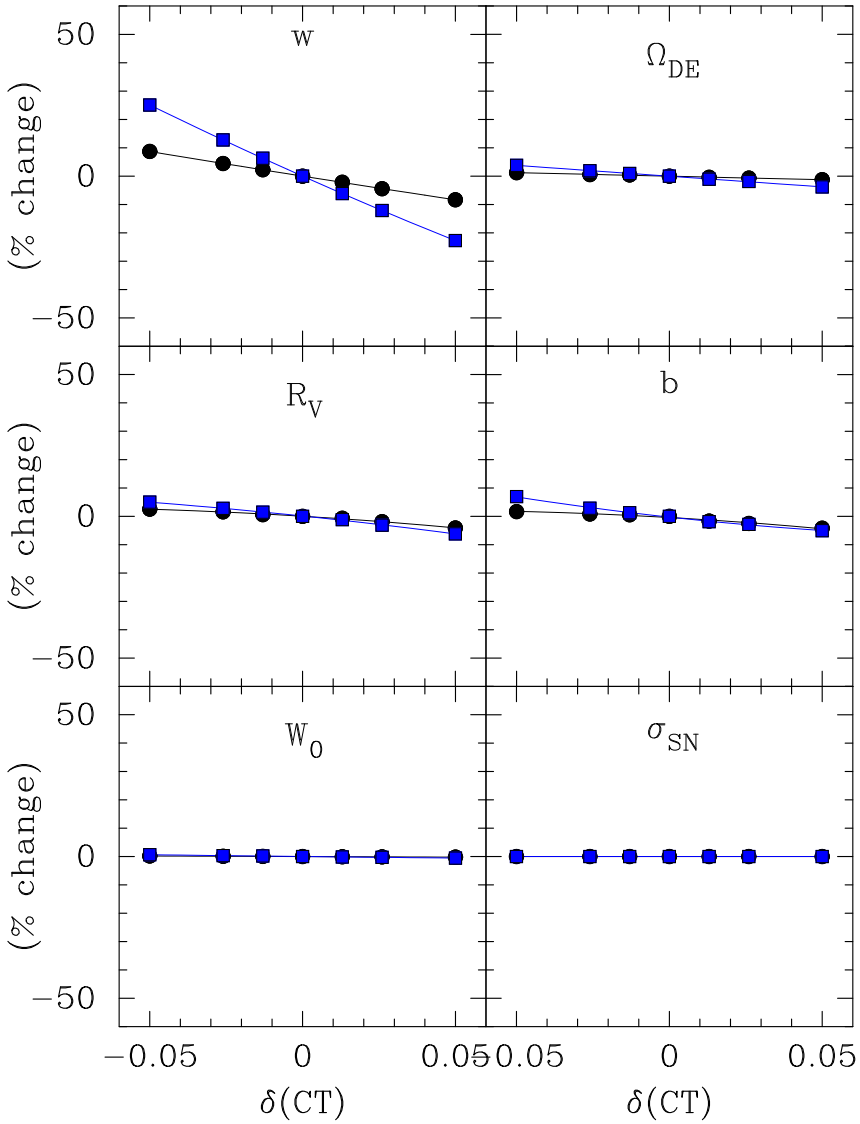


FIG. 23.— The effect of an error in the color-term derived from local sequences of standards, as listed in Figure 20. The black circles are for $i$-band, while the red squares are for $B$-band. The lines are quadratic fits. An error in the color term has the largest impact on $w$. For an error of 0.015, the percentage change in $w$ amounts to 3%.

TABLE 1
FILTER NOMENCLATURE

| Name | Eff. Wavelength (Angstroms) | Description | Zero-point | reference |
|---|---|---|---|---|
| $Y$ | 10333.6 | $Y$-band on PANIC, Magellan I, LCO | 12.6870 | Persson et al. (1998) |
| $J$ | 12440.3 | $J$-band on PANIC, Magellan I, LCO | 12.8520 | ” |
| $B$ | 4905.0 | $B$-band on Swope, LCO | 13.6672 | Hamuy et al. (2006) |
| $V$ | 4905.0 | $V$-band on Swope, LCO | 13.7758 | ” |
| $i$ | 4905.0 | $i$-band on Swope, LCO | 13.6873 | ” |
| $g_m$ | 4905.0 | $g$-band on Megacam, CFHT | 15.5363 | Astier et al. (2006) |
| $r_m$ | 6282.6 | $r$-band on Megacam, CFHT | 14.8061 | ” |
| $i_m$ | 7725.0 | $i$-band on Megacam, CFHT | 14.5543 | ” |
| $z_m$ | 8901.6 | $z$-band on Megacam, CFHT | 13.9996 | ” |
| $g_s$ | 4718.9 | $g$-band on 2.5m, APO | 14.2013 | Smith et al. (2002) |
| $r_s$ | 6185.2 | $r$-band on 2.5m, APO | 14.2157 | ” |
| $i_s$ | 7499.7 | $i$-band on 2.5m, APO | 13.7775 | ” |
| $R_{4m}$ | 6660.2 | $R$-band on 4m Blanco telescope, CTIO | 15.1820 | Miknaitis et al. (2007) |
| $I_{4m}$ | 7973.8 | $I$-band on 4m Blanco telescope, CTIO | 14.4580 | ” |

TABLE 2
CSP high-z SNe

| Name | RA (2000) (d:m:s) | DEC (2000) (h:m:s) | Epochs | z | Cross-ID |
|---|---|---|---|---|---|
| SNLS 03D4gl | 22:14:44.16 | -17:31:44.40 | 3 | 0.571 | ··· |
| SNLS 04D1oh | 02:25:02.38 | -04:14:10.68 | 2 | 0.59 | ··· |
| SNLS 04D1pg | 02:27:04.15 | -04:10:31.33 | 3 | 0.515 | ··· |
| SNLS 04D1rh | 02:27:47.16 | -04:15:13.68 | 4 | 0.435 | ··· |
| SNLS 04D1sk | 02:24:22.56 | -04:21:13.32 | 2 | 0.6634 | ··· |
| SNLS 04D2an | 10:00:52.32 | 02:02:28.68 | 8 | 0.62 | ··· |
| SNLS 05D1dn | 02:24:26.64 | -04:59:29.40 | 4 | 0.566 | ··· |
| SNLS 05D1hk | 02:24:39.17 | -04:38:03.01 | 2 | 0.2631 | ··· |
| SNLS 05D1hn | 02:24:36.26 | -04:10:54.95 | 1 | 0.1489 | ··· |
| SNLS 05D1ix | 02:24:19.94 | -04:40:11.75 | 3 | 0.49 | ··· |
| SNLS 05D1iy | 02:27:39.96 | -04:25:21.36 | 1 | 0.2478 | ··· |
| SNLS 05D2ah | 10:01:28.80 | 01:51:46.08 | 6 | 0.184 | ··· |
| SNLS 05D2bt | 10:01:40.32 | 02:33:57.96 | 5 | 0.679 | ··· |
| SNLS 05D2bv | 10:02:17.04 | 02:14:26.16 | 5 | 0.474 | ··· |
| SNLS 05D2ck | 10:00:45.12 | 02:34:22.08 | 4 | 0.698 | ··· |
| SNLS 05D2dw | 09:58:32.16 | 02:01:56.28 | 2 | 0.417 | ··· |
| SNLS 05D2eb | 10:00:14.64 | 02:24:26.64 | 2 | 0.5344 | ··· |
| SNLS 05D2mp | 09:59:08.64 | 02:12:14.69 | 3 | 0.3537 | ··· |
| SNLS 05D4cw | 22:14:50.16 | -17:44:19.32 | 3 | 0.375 | ··· |
| SNLS 05D4fo | 22:15:20.88 | -17:16:05.16 | 4 | 0.373 | ··· |
| ESS d149wcc4-11 | 02:10:53.98 | -04:25:49.80 | 3 | 0.342 | SN2003jy |
| ESS e108wdd8-4 | 02:30:09.00 | -09:04:35.76 | 3 | 0.469 | SN2003km |
| SDSS 12855 | 22:01:01.44 | 00:42:58.47 | 2 | 0.165 | ··· |
| SDSS 13025 | 22:46:16.08 | 00:24:57.21 | 3 | 0.224 | ··· |
| SDSS 13835 | 00:24:14.31 | -00:14:53.69 | 2 | 0.247 | ··· |
| SDSS 15287 | 21:35:50.40 | -01:03:26.75 | 1 | 0.235 | ··· |
| SDSS 16442 | 21:59:47.28 | -00:43:59.59 | 3 | 0.281 | ··· |
| SDSS 3241 | 20:50:36.24 | -00:21:14.76 | 5 | 0.259 | SN2005gh |
| SDSS 3331 | 02:18:14.74 | 00:47:47.76 | 5 | 0.208 | SN2005ge |
| SDSS 4679 | 01:26:06.79 | 00:40:36.80 | 4 | 0.333 | SN2205gy |
| SDSS 5183 | 03:33:48.96 | 00:42:33.70 | 6 | 0.384 | SN2005gq |
| SDSS 5549 | 00:13:00.13 | 00:14:53.70 | 5 | 0.119 | SN2005hx |
| SDSS 6699 | 21:31:15.60 | -01:03:25.16 | 4 | 0.311 | SN2005ik |
| SDSS 7243 | 21:52:18.96 | 00:28:19.09 | 3 | 0.204 | SN2005jm |
| SDSS 7512 | 03:28:21.67 | -00:19:34.10 | 2 | 0.22 | SN2005jo |

TABLE 3
CSP high-z Photometry

| Name | MJD[a] (days) | $Y_c$ (mag) | $\sigma_Y$ (mag) | $K_{Y,I}$[b] (mag) | $J_c$ (mag) | $\sigma_J$ (mag) | $K_{J,I}$[c] (mag) |
|---|---|---|---|---|---|---|---|
| SNLS 03D4gl | 52947.0 | 22.57 | 0.09 | -0.97 | 22.84 | 0.15 | -1.37 |
| | 52947.0 | 22.54 | 0.05 | -0.91 | 23.03 | 0.13 | -1.40 |
| | 52952.0 | 22.64 | 0.05 | -0.90 | 22.80 | 0.08 | -1.38 |
| SNLS 04D1oh | 53302.1 | ... | ... | ... | 22.81 | 0.09 | -1.39 |
| | 53314.2 | ... | ... | ... | 22.78 | 0.10 | -1.37 |
| SNLS 04D1pg | 53328.2 | ... | ... | ... | 22.72 | 0.08 | -1.46 |
| | 53338.1 | ... | ... | ... | 22.95 | 0.08 | -1.48 |
| | 53344.2 | ... | ... | ... | 23.28 | 0.19 | -1.59 |
| SNLS 04D1rh | 53356.1 | 22.44 | 0.06 | -1.21 | 22.26 | 0.07 | -1.34 |
| | 53356.1 | 22.60 | 0.09 | -1.23 | 22.53 | 0.11 | -1.46 |
| SNLS 04D1sk | 53356.1 | ... | ... | ... | 23.33 | 0.19 | -1.50 |
| | 53363.0 | ... | ... | ... | 23.78 | 0.33 | -1.51 |
| SNLS 04D2an | 53027.2 | 22.75 | 0.05 | -1.11 | 22.92 | 0.07 | -1.41 |
| | 53027.2 | 22.63 | 0.05 | -1.08 | 23.23 | 0.11 | -1.40 |
| | 53034.1 | 22.84 | 0.10 | -1.03 | 23.07 | 0.14 | -1.39 |
| | 53034.1 | 22.67 | 0.05 | -0.95 | 23.58 | 0.17 | -1.39 |
| | 53040.2 | 23.11 | 0.07 | -0.91 | 23.64 | 0.17 | -1.41 |
| | 53040.2 | 23.27 | 0.12 | -0.90 | 23.52 | 0.22 | -1.41 |
| | 53045.2 | 23.32 | 0.07 | -1.03 | 23.38 | 0.14 | -1.41 |
| | 53045.2 | 23.33 | 0.10 | -1.06 | 23.73 | 0.20 | -1.41 |
| SNLS 05D1dn | 53641.3 | ... | ... | ... | 22.76 | 0.13 | -1.35 |
| | 53654.3 | ... | ... | ... | 22.64 | 0.10 | -1.35 |
| | 53659.2 | ... | ... | ... | 22.94 | 0.13 | -1.36 |
| | 53666.2 | ... | ... | ... | 23.11 | 0.19 | -1.41 |
| SNLS 05D1hk | 53720.0 | 21.10 | 0.03 | -1.02 | ... | ... | ... |
| | 53724.1 | 21.13 | 0.03 | -0.98 | ... | ... | ... |
| SNLS 05D1hn | 53721.0 | 20.63 | 0.03 | -0.97 | ... | ... | ... |
| SNLS 05D1ix | 53720.1 | ... | ... | ... | 22.07 | 0.09 | -1.54 |
| | 53722.1 | ... | ... | ... | 22.27 | 0.09 | -1.54 |
| | 53724.0 | ... | ... | ... | 22.04 | 0.09 | -1.51 |
| SNLS 05D1iy | 53721.1 | 21.65 | 0.02 | -0.92 | ... | ... | ... |
| SNLS 05D2ah | 53390.2 | 20.84 | 0.03 | -0.86 | 21.46 | 0.05 | -0.39 |
| | 53390.2 | 20.93 | 0.02 | -0.87 | ... | ... | ... |
| | 53391.2 | ... | ... | ... | 21.71 | 0.06 | -0.38 |
| | 53392.2 | 20.93 | 0.02 | -0.92 | 21.71 | 0.08 | -0.37 |
| | 53393.3 | 21.02 | 0.03 | -0.95 | 21.77 | 0.07 | -0.37 |
| | 53393.3 | 20.93 | 0.02 | -1.16 | 21.66 | 0.04 | -0.37 |
| SNLS 05D2bt | 53405.1 | ... | ... | ... | 22.98 | 0.09 | -1.54 |
| | 53413.2 | ... | ... | ... | 23.28 | 0.24 | -1.55 |
| | 53418.1 | ... | ... | ... | 23.07 | 0.34 | -1.56 |
| | 53424.1 | ... | ... | ... | 23.47 | 0.28 | -1.54 |
| | 53430.1 | ... | ... | ... | 23.09 | 0.20 | -1.54 |
| SNLS 05D2bv | 53405.3 | ... | ... | ... | 22.21 | 0.04 | -1.35 |
| | 53413.2 | ... | ... | ... | 22.64 | 0.13 | -1.36 |
| | 53418.2 | ... | ... | ... | 22.58 | 0.08 | -1.41 |
| | 53424.2 | ... | ... | ... | 22.76 | 0.15 | -1.58 |
| | 53430.1 | ... | ... | ... | 22.90 | 0.14 | -1.60 |
| SNLS 05D2ck | 53418.3 | ... | ... | ... | 23.28 | 0.25 | -1.54 |
| | 53424.3 | ... | ... | ... | 23.29 | 0.30 | -1.58 |
| | 53430.2 | ... | ... | ... | 23.51 | 0.23 | -1.59 |
| | 53444.1 | ... | ... | ... | 23.61 | 0.20 | -1.55 |
| SNLS 05D2dw | 53447.1 | 21.99 | 0.07 | -1.16 | 22.20 | 0.09 | -1.31 |
| | 53447.1 | 22.20 | 0.06 | -1.14 | 22.00 | 0.06 | -1.30 |
| SNLS 05D2eb | 53447.1 | 22.23 | 0.12 | -0.82 | 22.40 | 0.15 | -1.51 |
| | 53447.1 | 22.49 | 0.04 | -0.78 | ... | ... | ... |
| SNLS 05D2mp | 53720.3 | 22.44 | 0.04 | -0.94 | ... | ... | ... |
| | 53722.2 | 22.55 | 0.04 | -0.95 | ... | ... | ... |
| | 53724.3 | 22.54 | 0.04 | -0.96 | ... | ... | ... |
| SNLS 05D4cw | 53591.1 | 22.35 | 0.07 | -1.01 | ... | ... | ... |
| | 53596.1 | 22.66 | 0.08 | -1.03 | ... | ... | ... |
| | 53608.1 | 22.55 | 0.08 | -1.05 | ... | ... | ... |
| SNLS 05D4fo | 53648.1 | 22.14 | 0.45 | -1.00 | 22.07 | 0.15 | -1.35 |
| | 53648.1 | 22.32 | 0.07 | -1.00 | 21.64 | 0.06 | -1.50 |
| | 53654.1 | 22.50 | 0.12 | -1.00 | 21.79 | 0.11 | -1.48 |
| | 53654.1 | 22.76 | 0.10 | -1.00 | 21.96 | 0.11 | -1.56 |
| ESS d149wcc4-11 | 52947.3 | 22.01 | 0.04 | -0.91 | ... | ... | ... |
| | 52952.2 | 21.92 | 0.03 | -0.92 | ... | ... | ... |
| | 52956.2 | 21.97 | 0.03 | -0.91 | ... | ... | ... |
| ESS e108wdd8-4 | 52980.1 | 22.42 | 0.04 | -1.29 | 22.25 | 0.08 | -1.38 |
| | 52980.1 | 22.24 | 0.03 | -1.30 | 22.28 | 0.09 | -1.39 |
| | 52982.1 | 22.20 | 0.03 | -1.31 | 22.28 | 0.08 | -1.39 |
| SDSS 12855 | 54000.1 | 20.61 | 0.02 | -0.89 | ... | ... | ... |
| | 54008.0 | 20.92 | 0.02 | -1.10 | ... | ... | ... |
| SDSS 13025 | 53996.1 | 21.02 | 0.03 | -1.00 | ... | ... | ... |

TABLE 3 — *Continued*

| Name | MJD[a] (days) | $Y_c$ (mag) | $\sigma_Y$ (mag) | $K_{Y,I}$[b] (mag) | $J_c$ (mag) | $\sigma_J$ (mag) | $K_{J,I}$[c] (mag) |
|---|---|---|---|---|---|---|---|
| | 54000.1 | 21.08 | 0.04 | -0.99 | ... | ... | ... |
| | 54008.1 | 21.58 | 0.04 | -1.20 | ... | ... | ... |
| SDSS 13835 | 54008.1 | 21.14 | 0.01 | -0.90 | ... | ... | ... |
| | 54021.2 | 21.40 | 0.02 | -1.01 | ... | ... | ... |
| SDSS 15287 | 54029.0 | 21.13 | 0.02 | -0.94 | ... | ... | ... |
| SDSS 16442 | 54060.0 | 21.30 | 0.04 | -0.86 | ... | ... | ... |
| | 54065.0 | 21.46 | 0.03 | -0.80 | ... | ... | ... |
| | 54070.0 | 21.79 | 0.04 | -0.80 | ... | ... | ... |
| SDSS 3241 | 53641.0 | 21.31 | 0.02 | -0.86 | ... | ... | ... |
| | 53648.0 | 21.27 | 0.02 | -0.93 | ... | ... | ... |
| | 53654.0 | 21.54 | 0.02 | -0.90 | ... | ... | ... |
| | 53659.0 | 21.79 | 0.02 | -0.95 | ... | ... | ... |
| | 53666.0 | 21.98 | 0.03 | -1.05 | ... | ... | ... |
| SDSS 3331 | 53641.2 | 20.80 | 0.03 | -0.88 | ... | ... | ... |
| | 53648.3 | 20.50 | 0.04 | -1.06 | ... | ... | ... |
| | 53655.2 | 20.77 | 0.03 | -1.03 | ... | ... | ... |
| | 53659.2 | 20.82 | 0.03 | -1.10 | ... | ... | ... |
| | 53676.2 | 20.89 | 0.04 | -1.32 | ... | ... | ... |
| SDSS 4679 | 53655.1 | 21.99 | 0.02 | -0.89 | ... | ... | ... |
| | 53659.1 | 22.02 | 0.03 | -0.88 | ... | ... | ... |
| | 53666.2 | 22.35 | 0.04 | -0.89 | ... | ... | ... |
| | 53676.2 | 22.37 | 0.03 | -0.91 | ... | ... | ... |
| SDSS 5183 | 53654.3 | 22.39 | 0.06 | -1.03 | ... | ... | ... |
| | 53655.3 | 22.46 | 0.05 | -1.04 | ... | ... | ... |
| | 53666.2 | 23.22 | 0.09 | -1.04 | ... | ... | ... |
| | 53676.3 | 22.94 | 0.07 | -1.06 | ... | ... | ... |
| | 53720.2 | 23.68 | 0.14 | -1.09 | ... | ... | ... |
| | 53721.2 | 23.72 | 0.16 | -1.09 | ... | ... | ... |
| SDSS 5549 | 53666.1 | 19.88 | 0.04 | -0.56 | ... | ... | ... |
| | 53676.1 | 20.20 | 0.04 | -0.65 | ... | ... | ... |
| | 53682.1 | 20.03 | 0.11 | -0.93 | ... | ... | ... |
| | 53684.1 | 20.18 | 0.03 | -0.95 | ... | ... | ... |
| | 53689.1 | 20.11 | 0.04 | -0.97 | ... | ... | ... |
| SDSS 6699 | 53676.0 | 21.72 | 0.02 | -0.90 | ... | ... | ... |
| | 53682.0 | 21.87 | 0.05 | -0.85 | ... | ... | ... |
| | 53684.0 | 22.16 | 0.04 | -0.84 | ... | ... | ... |
| | 53689.0 | 22.42 | 0.05 | -0.85 | ... | ... | ... |
| SDSS 7243 | 53682.1 | 20.82 | 0.02 | -0.83 | ... | ... | ... |
| | 53684.1 | 20.87 | 0.02 | -0.88 | ... | ... | ... |
| | 53689.0 | 20.94 | 0.01 | -0.88 | ... | ... | ... |
| SDSS 7512 | 53682.3 | 21.21 | 0.10 | -0.89 | ... | ... | ... |
| | 53684.3 | 21.25 | 0.07 | -0.89 | ... | ... | ... |

[a] MJD = JD - 2400000.5.

[b] K-correction from observed filter $Y_c$ to rest-frame filter I.

[c] K-correction from observed filter $J_c$ to rest-frame filter I, except for SNLS05D2ah, for which the K-correction is to rest-frame Y.

TABLE 4
Derived Light-curve Parameters for low-z SNe

| Name | z | $\mu$ ($\sigma$)[a] (mag) | $T_{max}(\sigma)$[b] (days) | $\Delta m_{15}(\sigma)$[c] (mag) | $(i_{max})$ ($\sigma$)[d] (mag) | $(B_{max} - V_{max})$ ($\sigma$)[d] (mag) | $E(B-V)_{host}$ ($\sigma$)[e] (mag) | $A_{TOT}$[f] (mag) |
|---|---|---|---|---|---|---|---|---|
| SN2004ef | 0.03097 | 35.499(0.139) | 264.8(0.0) | 1.389(0.007) | 17.273(0.010) | 0.123 (0.007) | 0.157 (0.018) | 0.214 |
| SN2004eo | 0.01569 | 33.697(0.189) | 278.9(0.1) | 1.366(0.012) | 15.435(0.016) | 0.095 (0.015) | 0.129 (0.021) | 0.249 |
| SN2004ey | 0.01578 | 34.027(0.190) | 304.6(0.0) | 0.954(0.006) | 15.459(0.011) | -0.070 (0.008) | -0.003 (0.015) | 0.163 |
| SN2004gs | 0.02663 | 35.484(0.142) | 356.3(0.0) | 1.550(0.006) | 17.391(0.009) | 0.202 (0.009) | 0.223 (0.022) | 0.247 |
| SN2004gu | 0.04583 | 36.484(0.129) | 362.1(0.2) | 0.758(0.011) | 18.052(0.020) | 0.145 (0.021) | 0.253 (0.027) | 0.268 |
| SN2005ag | 0.07937 | 37.643(0.121) | 414.1(0.1) | 0.889(0.007) | 19.123(0.011) | 0.004 (0.007) | 0.085 (0.016) | 0.128 |
| SN2005al | 0.01239 | 34.092(0.202) | 430.6(0.1) | 1.243(0.010) | 15.609(0.015) | -0.089 (0.009) | -0.057 (0.016) | 0.012 |
| SN2005el | 0.01490 | 33.967(0.189) | 647.0(0.1) | 1.299(0.014) | 15.538(0.018) | -0.055 (0.014) | -0.025 (0.020) | 0.112 |
| SN2005eq | 0.02896 | 35.489(0.141) | 654.5(0.1) | 0.778(0.008) | 16.962(0.015) | 0.039 (0.010) | 0.135 (0.020) | 0.215 |
| SN2005hc | 0.04591 | 36.582(0.128) | 667.4(0.1) | 0.844(0.008) | 18.050(0.014) | 0.009 (0.008) | 0.095 (0.017) | 0.129 |
| SN2005hj | 0.05797 | 36.976(0.127) | 674.0(0.2) | 0.739(0.017) | 18.462(0.026) | 0.067 (0.014) | 0.170 (0.023) | 0.207 |
| SN2005iq | 0.03402 | 35.891(0.136) | 687.9(0.1) | 1.230(0.016) | 17.457(0.019) | -0.033 (0.011) | 0.005 (0.017) | 0.032 |
| SN2005ir | 0.07631 | 37.589(0.127) | 685.0(0.2) | 0.875(0.025) | 19.086(0.037) | 0.027 (0.016) | 0.112 (0.022) | 0.141 |
| SN2005kc | 0.01511 | 33.871(0.197) | 698.3(0.0) | 1.150(0.016) | 15.632(0.020) | 0.200 (0.014) | 0.267 (0.019) | 0.409 |
| SN2005ki | 0.01919 | 34.615(0.159) | 705.9(0.0) | 1.381(0.007) | 16.237(0.010) | -0.031 (0.010) | -0.010 (0.019) | 0.029 |
| SN2005M | 0.02200 | 35.052(0.151) | 405.9(0.0) | 0.799(0.003) | 16.518(0.006) | 0.024 (0.004) | 0.117 (0.017) | 0.146 |
| SN2005na | 0.02630 | 35.118(0.145) | 740.3(0.2) | 1.005(0.013) | 16.618(0.020) | -0.018 (0.015) | 0.048 (0.019) | 0.137 |
| SN2006ax | 0.01673 | 34.324(0.169) | 827.5(0.1) | 0.949(0.008) | 15.763(0.014) | -0.060 (0.011) | 0.009 (0.017) | 0.068 |
| SN2006bh | 0.01084 | 33.329(0.238) | 833.6(0.0) | 1.387(0.008) | 14.977(0.010) | -0.007 (0.009) | 0.016 (0.018) | 0.047 |
| SN2006gt | 0.04474 | 36.441(0.130) | 1003.0(0.1) | 1.675(0.012) | 18.415(0.020) | 0.225 (0.020) | 0.234 (0.031) | 0.264 |
| SN2006py | 0.05786 | 36.839(0.137) | 1071.0(0.3) | 1.016(0.049) | 18.421(0.060) | 0.070 (0.021) | 0.142 (0.025) | 0.205 |

[a] Distance modulus ($h = 0.72$).
[b] Time of maximum for rest-frame B light-curve (JD - 2400000.5).
[c] Decline rate parameter.
[d] Galactic reddening from Schlegel et al. (1998).
[e] Host galaxy reddening assuming Phillips et al. (1999) colors.
[f] Total (galactic + host galaxy) absorption in NIR toward SN assuming $R_V = 1.7$.

TABLE 5
Derived Light-curve Parameters

| Name | z | $\mu$ ($\sigma$)[a] (mag) | $T_{max}(\sigma)$[b] (days) | $\Delta m_{15}(\sigma)$[c] (mag) | $(i_{max})$ ($\sigma$)[d] (mag) | $(B_{max} - V_{max})$ ($\sigma$)[d] (mag) | $E(B-V)_{host}$ ($\sigma$)[e] (mag) | $A_{TOT}$[f] (mag) |
|---|---|---|---|---|---|---|---|---|
| SNLS 03D4gl | 0.571 | 42.765(0.170) | 52954.1(0.6) | 0.719(0.151) | 24.192(0.120) | 0.020 (0.029) | 0.122 (0.038) | 0.136 |
| SNLS 04D1oh | 0.59 | 42.680(0.180) | 53306.9(0.4) | 0.946(0.069) | 24.070(0.087) | -0.026 (0.056) | 0.046 (0.058) | 0.067 |
| SNLS 04D1pg | 0.515 | 42.353(0.148) | 53325.5(0.3) | 0.813(0.050) | 24.059(0.078) | 0.138 (0.029) | 0.238 (0.034) | 0.248 |
| SNLS 04D1rh | 0.435 | 41.942(0.134) | 53349.2(0.4) | 0.877(0.048) | 23.353(0.069) | -0.007 (0.019) | 0.074 (0.024) | 0.100 |
| SNLS 04D1sk | 0.6634 | 43.307(0.227) | 53354.6(0.7) | 1.399(0.109) | 24.810(0.153) | -0.032 (0.062) | -0.013 (0.066) | 0.011 |
| SNLS 04D2an | 0.62 | 42.957(0.151) | 53031.0(0.8) | 0.872(0.098) | 24.347(0.110) | ... | ... | ... |
| SNLS 05D1dn | 0.566 | 42.417(0.153) | 53647.3(0.6) | 0.742(0.044) | 23.941(0.091) | 0.062 (0.031) | 0.165 (0.036) | 0.181 |
| SNLS 05D1hk | 0.2631 | 40.438(0.176) | 53718.1(0.3) | 0.889(0.029) | 21.926(0.136) | 0.027 (0.014) | 0.109 (0.021) | 0.130 |
| SNLS 05D1hn | 0.1489 | 39.128(0.244) | 53713.2(0.1) | 0.850(0.038) | 21.231(0.219) | 0.317 (0.020) | 0.428 (0.026) | 0.436 |
| SNLS 05D1ix | 0.49 | 42.022(0.131) | 53718.6(0.0) | 0.896(0.017) | 23.526(0.070) | 0.034 (0.006) | 0.116 (0.016) | 0.133 |
| SNLS 05D1iy | 0.2478 | 40.509(0.149) | 53715.5(0.1) | 1.191(0.041) | 22.216(0.096) | 0.089 (0.017) | 0.142 (0.021) | 0.165 |
| SNLS 05D2ah | 0.184 | 39.656(0.104) | 53382.5(0.0) | 0.995(0.010) | 21.310(0.016) | 0.090 (0.005) | 0.166 (0.014) | 0.178 |
| SNLS 05D2bt | 0.679 | 43.169(0.189) | 53400.8(0.3) | 0.941(0.076) | 24.306(0.115) | -0.142 (0.051) | -0.080 (0.054) | -0.056 |
| SNLS 05D2bv | 0.474 | 42.194(0.131) | 53403.8(0.1) | 1.031(0.037) | 23.471(0.065) | -0.089 (0.011) | -0.033 (0.017) | -0.016 |
| SNLS 05D2ck | 0.698 | 43.088(0.256) | 53415.7(0.8) | 1.644(0.108) | 24.721(0.103) | -0.004 (0.097) | -0.010 (0.101) | 0.006 |
| SNLS 05D2dw | 0.417 | 41.933(0.123) | 53453.3(0.1) | 0.879(0.029) | 23.240(0.059) | -0.056 (0.013) | 0.021 (0.020) | 0.043 |
| SNLS 05D2eb | 0.5344 | 42.376(0.218) | 53450.4(0.4) | 0.836(0.056) | 23.885(0.182) | 0.043 (0.024) | 0.133 (0.030) | 0.140 |
| SNLS 05D2mp | 0.3537 | 41.577(0.115) | 53710.2(0.1) | 0.804(0.014) | 23.018(0.054) | 0.016 (0.010) | 0.108 (0.019) | 0.125 |
| SNLS 05D4cw | 0.375 | 41.394(0.174) | 53581.0(0.9) | 1.396(0.126) | 22.920(0.097) | -0.021 (0.048) | -0.000 (0.053) | 0.030 |
| SNLS 05D4fo | 0.373 | 41.689(0.120) | 53658.0(0.1) | 1.269(0.025) | 23.232(0.063) | 0.003 (0.011) | 0.041 (0.018) | 0.069 |
| ESS d149wcc4-11 | 0.342 | 41.337(0.121) | 52955.3(0.3) | 0.894(0.045) | 22.791(0.038) | 0.011 (0.026) | 0.091 (0.030) | 0.110 |
| ESS e108wdd8-4 | 0.469 | 42.391(0.176) | 52980.6(0.8) | 0.516(0.107) | 23.469(0.092) | -0.115 (0.047) | -0.001 (0.055) | 0.028 |
| SDSS 12855 | 0.165 | 39.423(0.175) | 53995.5(0.3) | 1.347(0.079) | 21.209(0.024) | 0.105 (0.041) | 0.142 (0.045) | 0.196 |
| SDSS 13025 | 0.224 | 40.019(0.186) | 53993.2(0.8) | 1.047(0.089) | 21.783(0.081) | 0.134 (0.047) | 0.208 (0.050) | 0.289 |
| SDSS 13835 | 0.247 | 40.635(0.156) | 54011.0(0.6) | 0.816(0.054) | 22.002(0.043) | -0.020 (0.037) | 0.067 (0.041) | 0.093 |
| SDSS 15287 | 0.235 | 40.614(0.156) | 54028.6(0.4) | 0.820(0.065) | 21.968(0.056) | -0.026 (0.031) | 0.060 (0.035) | 0.112 |
| SDSS 16442 | 0.281 | 40.217(0.271) | 54060.2(1.0) | 1.042(0.143) | 21.983(0.143) | 0.136 (0.092) | 0.210 (0.094) | 0.284 |
| SDSS 3241 | 0.259 | 40.827(0.197) | 53647.2(0.4) | 1.005(0.056) | 21.970(0.053) | -0.148 (0.067) | -0.093 (0.069) | 0.079 |
| SDSS 3331 | 0.208 | 39.746(0.182) | 53649.5(0.4) | 0.922(0.070) | 21.479(0.064) | 0.136 (0.046) | 0.224 (0.048) | 0.255 |
| SDSS 4679 | 0.333 | 41.454(0.235) | 53652.7(0.6) | 0.704(0.052) | 22.734(0.064) | -0.045 (0.093) | 0.052 (0.095) | 0.084 |
| SDSS 5183 | 0.384 | 42.069(0.390) | 53649.3(1.3) | 0.946(0.130) | 23.149(0.133) | -0.170 (0.163) | -0.110 (0.164) | 0.042 |
| SDSS 5549 | 0.119 | 38.745(0.123) | 53665.5(0.4) | 0.920(0.047) | 20.333(0.054) | 0.069 (0.022) | 0.152 (0.026) | 0.182 |
| SDSS 6699 | 0.311 | 41.063(0.194) | 53675.4(0.6) | 1.075(0.081) | 22.468(0.070) | -0.036 (0.067) | 0.021 (0.069) | 0.085 |
| SDSS 7243 | 0.204 | 40.148(0.170) | 53685.7(0.2) | 0.929(0.066) | 21.561(0.053) | -0.013 (0.037) | 0.062 (0.040) | 0.178 |
| SDSS 7512 | 0.22 | 40.353(0.203) | 53681.8(0.4) | 0.967(0.112) | 21.902(0.114) | 0.045 (0.047) | 0.121 (0.050) | 0.235 |

[a] Distance modulus ($h = 0.72$).
[b] Time of maximum for rest-frame B light-curve (JD - 2400000.5).
[c] Decline rate parameter.
[d] Galactic reddening from Schlegel et al. (1998).
[e] Host galaxy reddening assuming Phillips et al. (1999) colors.
[f] Total (galactic + host galaxy) absorption in NIR toward SN assuming $R_V = 1.7$.

TABLE 6
Binned Hubble Diagram

| $< z >$ | N | $< \mu >$ | $\sigma(\mu)$ |
|---|---|---|---|
| 0.01 | 6 | 33.906 | 0.018 |
| 0.02 | 3 | 34.635 | 0.049 |
| 0.03 | 5 | 35.505 | 0.028 |
| 0.05 | 5 | 36.619 | 0.032 |
| 0.08 | 2 | 37.595 | 0.045 |
| 0.13 | 2 | 38.930 | 0.117 |
| 0.17 | 2 | 39.627 | 0.099 |
| 0.24 | 10 | 40.357 | 0.054 |
| 0.35 | 7 | 41.397 | 0.057 |
| 0.46 | 5 | 41.984 | 0.065 |
| 0.56 | 5 | 42.543 | 0.075 |
| 0.68 | 3 | 43.023 | 0.107 |

TABLE 7
Cosmological Results

| $R_V$ | Band | $\Omega_m$ | $w$ | $rms$ |
|---|---|---|---|---|
| 1.74 | $W^{i'}_{BV}$ | $0.27 \pm 0.02$ | $-1.05 \pm 0.13$ | 0.13 |
| | $W^{B}_{BV}$ | $0.27 \pm 0.02$ | $-1.08 \pm 0.14$ | 0.15 |
| 3.1 | $W^{i'}_{BV}$ | $0.26 \pm 0.02$ | $-1.20 \pm 0.13$ | 0.20 |
| | $W^{B}_{BV}$ | $0.25 \pm 0.03$ | $-1.24 \pm 0.16$ | 0.24 |

TABLE 8
Systematic Errors

| | | $\Omega_k = 0$ | | $w = -1$ | | $j$ =constant | | | | nuisance | | | | | |
|---|---|---|---|---|---|---|---|---|---|---|---|---|---|---|---|
| Systematic | Error | $\frac{dw}{d\sigma}$ | $\Delta w$ | $\frac{d\Omega_{DE}}{d\sigma}$ | $\Delta\Omega_{DE}$ | $\frac{dq_0}{d\sigma}$ | $\Delta q_0$ | $\frac{dj_k}{d\sigma}$ | $\Delta j_k$ | $\frac{dR_V}{d\sigma}$ | $\Delta R_V$ | $\frac{db}{d\sigma}$ | $\Delta b$ | $\frac{dW_0}{d\sigma}$ | $\Delta W_0$ |
| Mag. offset ($\delta m$) | 0.025 | -2.69 | 0.067 | 2.73 | 0.068 | -2.75 | 0.069 | 8.10 | 0.203 | 0.04 | 0.001 | 0.002 | 0.000 | -0.25 | 0.006 |
| Color offset ($\delta c$) | 0.02 | 2.53 | 0.051 | -2.58 | 0.052 | 2.68 | 0.054 | -7.77 | 0.155 | 0.38 | 0.008 | -0.03 | 0.001 | 0.21 | 0.004 |
| Color Term ($\delta(CT)$) | 0.015 | 1.8 | 0.027 | -1.73 | 0.026 | 1.83 | 0.027 | -5.82 | 0.087 | -0.67 | 0.010 | -0.22 | 0.003 | 0.71 | 0.011 |
| $\Delta m_{15}$ variance ($\sigma_\Delta$) | 0.05 | -0.007 | 0.000 | -0.01 | 0.001 | -0.04 | 0.002 | 0.14 | 0.007 | 0.09 | 0.005 | -0.06 | 0.003 | -0.03 | 0.002 |
| Color variance ($\sigma_c$) | 0.03 | 0.03 | 0.001 | 0.52 | 0.016 | -0.173 | 0.005 | 0.53 | 0.016 | ... | 0.100 | ... | 0.011 | ... | 0.004 |
| Total | | | 0.088 | | 0.091 | | 0.092 | | 0.270 | | 0.097 | | 0.012 | | 0.014 |

TABLE 9
Summary of Cosmological Parameters

| Constraints | Cosmological Parameters |
|---|---|
| $w = -1$ | $\Omega_m = 0.27 \pm 0.02$ (statistical) |
| Combine with BAO | $\Omega_{DE} = 0.76 \pm 0.13$ (statistical) $\pm 0.09$ (systematic) |
| $\Omega_k = 0$ | $\Omega_m = 0.27 \pm 0.03$ (statistical) |
| Combine with BAO | $w = -1.05 \pm 0.13$ (statistical) $\pm 0.09$ (systematic) |
| Constant j | $q_o = -0.67 \pm 0.13$ (statistical) $\pm 0.09$ (systematic) |
| Combine with BAO | $j_k = 1.18 \pm 0.44$ (statistical) $\pm 0.27$ (systematic) |